

The Sonora Brown Dwarf Atmosphere and Evolution Models. I. Model Description and Application to Cloudless Atmospheres in Rainout Chemical Equilibrium

Mark S. Marley 1 Didier Saumon 2 Channon Visscher Roxana Lupu 4 Roxana Freedman Rorley 6 Adam J. Roxana Lupu 4 Roxana Lupu 7 Adam J. Roxana Lupu 8 Planetary Laboratory, University of Arizona, Tucson, AZ 85721, USA; marley@lpl.arizona.edu

Lunar & Planetary Laboratory, University of Arizona, Tucson, AZ 85721, USA; marley@lpl.arizona.edu

Lunar & Planetary Laboratory, PO Box 1663, Los Alamos, NM 87545, USA

Dordt University, Sioux Center IA, Space Science Institute, Boulder, CO 80301, USA

BAER Institute, NASA Ames Research Center, Moffett Field, CA 94035, USA

SETI Institute, NASA Ames Research Center, Moffett Field, CA 94035, USA

Department of Astronomy, University of Texas at Austin, Austin, TX 78712, USA

Department of Astronomy & Astrophysics, University of California, Santa Cruz, CA 95064, USA

Leiden Observatory, Leiden, The Netherlands

Department of Astronomy, New Mexico State University, Las Cruces, NM 88003 USA

Department of Astronomy, University of Maryland, College Park, MD 20742, USA

1 Department of Physics and Astronomy, University of Leicester, Leicester, UK

Received 2021 March 5; revised 2021 July 8; accepted 2021 July 12; published 2021 October 18

Abstract

We present a new generation of substellar atmosphere and evolution models, appropriate for application to studies of L-, T-, and Y-type brown dwarfs and self-luminous extrasolar planets. The models describe the expected temperature-pressure profiles and emergent spectra of atmospheres in radiative-convective equilibrium with effective temperatures and gravities within the ranges $200 \leqslant T_{\rm eff} \leqslant 2400~{\rm K}$ and $2.5 \leqslant \log g \leqslant 5.5$. These ranges encompass masses from about 0.5 to 85 Jupiter masses for a set of metallicities ([M/H] = -0.5 to +0.5), C/O ratios (from 0.5 to 1.5 times that of solar), and ages. These models expand the diversity of model atmospheres currently available, notably to cooler effective temperatures and greater ranges in C/O. Notable improvements from past such models include updated opacities and atmospheric chemistry. Here we describe our modeling approach and present our initial tranche of models for cloudless, chemical equilibrium atmospheres. We compare the modeled spectra, photometry, and evolution to various data sets.

Unified Astronomy Thesaurus concepts: Brown dwarfs (185); T dwarfs (1679); L dwarfs (894); L subdwarfs (896); T subdwarfs (1680); Y dwarfs (1827); Stellar atmospheres (1584)

1. Introduction

The twenty-five years following the discovery of the first indisputable brown dwarf, Gliese 229 B (Oppenheimer et al. 1995), have seen a flowering of this field. Thousands of brown dwarfs have been discovered and characterized by spectroscopy and photometry (Joergens 2014). Dynamical masses and parallaxes have been measured for many objects and a wealth of trends uncovered (e.g., Dupuy & Liu 2017; Best et al. 2020). In addition, young, self-luminous planets have been discovered and characterized (e.g., Marois et al. 2008).

Most of these objects have been characterized with the help of forward modeling in which modelers construct hundreds to thousands of "grid models." The models, relying upon fundamental physical processes, predict spectral and evolutionary characteristics of brown dwarfs for given choices of intrinsic parameters, such as mass, age, and bulk composition. This approach typically relies upon both one-dimensional radiativeconvective equilibrium atmosphere models and coupled interior and evolution models. The atmosphere models aim to capture the key influences on substellar atmospheres, including chemistry, dynamics, and cloud processes in order to compute the vertical structure of an atmosphere which conservatively transports energy upwards from the deep interior. Evolution models apply the rate of energy loss through the atmosphere as a boundary condition in order to compute the evolution of radius and luminosity through time.

Such a forward modeling approach provides a self-consistent solution for the coupled problem of understanding both atmospheric and interior physical processes. By making predictions, models inform observers of interesting observational tests and connect observable properties, including luminosity and the spectral energy distribution, to the physical properties of the object, including mass and age. Grids of models are also essential for motivating and planning new observations. A non-exhaustive list of forward model grids includes those of Burrows et al. (1997), Baraffe et al. (2003), Saumon & Marley (2008), Allard et al. (2014), Baraffe et al. (2015), Malik et al. (2017), and Phillips et al. (2020).

The older models in the literature are generally out of date as our knowledge of molecular opacities, most notably water and methane, which are important absorbers in substellar atmospheres, has progressed substantially over the intervening years. Several of the more recent grid models use updated opacities but are generally not coupled with self-consistent evolution calculations, and thus do not provide a self-consistent evolutionary-atmospheric modeling framework, a notable exception being Phillips et al. (2020) and the ATMO2020 grid. Here we also provide such a framework, presenting coupled atmospheric structure and evolution models for a variety of atmospheric chemical assumptions. This effort is the first in an expected series of papers, each looking at additional model complexities, including disequilibrium chemistry, clouds, and so on. Independent modeling efforts, such as our own and that of Phillips et al. (2020), are crucial for crosschecking the importance of various physical and chemical assumptions and for overall self-consistency. Thus, we view the Sonora and ATMO2020 model sets to be highly complementary.

Further comparisons to some of the other model sets are discussed in Section 2.6.

In the past few years "retrieval methods," originally developed to study planetary atmospheres, have been applied to brown dwarfs (e.g., Line et al. 2015, 2017; Kitzmann et al. 2020; Piette & Madhusudhan 2020; Burningham et al. 2021) in order to understand the constraints on mass, luminosity, composition, radius, and other characteristics which are evident in the spectra alone, without resorting to underlying assumptions, such as solar abundance ratios, chemical equilibrium, and a radiative-convective structure. Retrievals excel at testing theoretical predictions by comparing a host of models to data, while accounting for various data set uncertainties. Retrieval methods are of greatest utility when judged in the context of grid model predictions as such comparisons test our understanding of underlying processes. By utilizing retrieval techniques, Line et al. (2017) and Zalesky et al. (2019), for example, unambiguously confirmed that rainout, not pure equilibrium, chemistry acts in substellar atmospheres (see further discussion in Section 2.5).

Both types of models are needed to motivate and interpret observations. In order to provide a new, systematic survey of brown dwarf atmospheric structure, emergent spectra, and evolution, we have constructed a new grid of brown dwarf model atmospheres. We ultimately aim for our grid to span broad ranges of atmospheric metallicity, C/O ratios, cloud properties, atmospheric mixing, and other parameters. Spectra predicted by our modeling grid can be compared to both observations and retrieval results to aid in the interpretation and planning of future telescopic observations.

For simplicity we divide the presentation of our new models into parts. Here, in Paper I we present our overall modeling approach, describing our atmosphere and evolution models as well as various model inputs, including opacities, and present results for cloudless models. In forthcoming papers in this series we will investigate disequilibrium chemistry and cloudy atmospheres. We break with previous tradition of our team by naming the models to provide clarity as to model generations. These and future models from our group are given the moniker "Sonora" after the desert spanning the southwestern United States and northern Mexico. Individual model generations (e.g., with a given set of opacities) will be denoted by names of flora and fauna of that desert. The cloudless, rainout chemical equilibrium models presented here are termed "Sonora Bobcat."

This paper describes our radiative-convective forward model for calculating the atmospheric structure of substellar objects and our evolution calculation for computing their trajectory through time. Section 2 describes the modeling details, Section 3 model results, and Section 4 highlights a few comparisons of model predictions to various data sets.

2. Model Description

We begin with a description of the atmospheric forward modeling approach. Here we term a forward model as a description of the variation of atmospheric temperature, T, and composition as a function of pressure, P, for a specified gravity, g, and effective temperature, $T_{\rm eff}$. In addition we specify the atmospheric metallicity and carbon-to-oxygen ratio. In future work we will describe additional constraints, including cloud treatments and vertical mixing.

Table 1 Model Parameters

Parameter	Range	Step
gravity	$3 \leqslant \log g \leqslant 5.5$	0.25
effective temperature	$200 \leqslant T_{\rm eff} \leqslant 2400 \; \rm K$	25 (≤600), 50 (≤1000), 100 (>1000 K)
metallicity	$-0.5 \le [M/H] \le +0.50$	0.25
carbon-to-oxygen ratio	$0.25 \leqslant (C/O)/(C/O)_{\odot} \leqslant 1.50$	0.25

Ultimately the selection of parameters and numerical approach employed in forward model grids depends on a series of judgment calls that balance the need for as precise as possible modeling of physical processes with numerical expediency. In this section we describe our approach to atmospheric modeling and briefly compare our choices to those of some other well known modeling schools. For a broader overview and literature survey of the substellar and planetary atmosphere modeling process, see the review by Marley & Robinson (2015).

2.1. Overview

Each model case is described by a limited set of specific parameters for 1D, plane-parallel atmospheres. For the initial model set presented here, these are gravity, g (presumed constant with height as the thickness of the atmosphere is much less than the body's radius), effective temperature, $T_{\rm eff}$, cloud treatment, metallicity [M/H], and carbon-to-oxygen (C/O) ratio. A crucial detail is that the abundance measures refer to the bulk chemistry of the gas from which the atmosphere forms. Various condensation processes can alter the atmosphere at any arbitrary pressure and temperature away from the bulk values by the removal of elements from the gas phase. For example, the condensation of magnesium silicates can sequester up to $\sim 20\%$ of the atmospheric oxygen inventory (in a solar-composition gas). This may yield a C/O ratio in the observable atmosphere of an object that is greater than its bulk C/O ratio if some oxygen has been removed by condensation processes deeper in its atmosphere (and if carbon has not likewise been removed by condensation processes of its own). We have selected a range of model parameters, shown in Table 1, to span that expected for the evolution of solarneighborhood ultracool dwarfs. Not all model combinations, particularly high-g, low $T_{\rm eff}$, are meaningful as the most massive, high-gravity objects will not have cooled to the lowest effective temperatures in the age of the universe.

While we account for the effect of condensation on the atmospheric composition and chemistry, here we set all condensate opacity equal to zero; cloudy models will be presented in an upcoming paper. In the future we will add additional standard parameters, such as cloud coverage fraction or eddy-mixing coefficient. For each combination of specific parameters we iteratively compute a single radiative-convective equilibrium atmosphere model. Such a model describes the variation in atmospheric temperature T as a function of pressure P. Given this T(P) profile and the abundances of all atmospheric constituents we can post-process emergent spectra at any needed spectral resolution.

2.2. Radiative-convective Equilibrium Model

Because the dominant sources of atmospheric opacity, such as H₂O, vary strongly with wavelength–particularly in cloud-free models such as these-the opacity of a gas column from a given depth in the atmosphere to infinity varies strongly with wavelength. A parcel of gas of a given temperature in the deep atmosphere can first radiate to space only over a narrow wavelength range, typically in the low opacity windows within Y or J bands. The atmosphere begins to emit strongly if the local Planck function overlaps these opacity windows. If sufficient energy can be radiated away, the local temperature lapse rate will transition from essentially adiabatic to the local radiative lapse rate. However, at higher, cooler levels in the atmosphere, the Planck function shifts to longer wavelengths where it can again encounter a high optical depth to infinity and the radiative lapse rate steepens as a result, in some cases enough to once more trigger convection. In very cool models ($T_{\rm eff}$ < 500 K) this process can repeat once more, leading to a stacked structure of up to three convective zones separated by radiative zones (Marley et al. 1996; Burrows et al. 1997; Morley et al. 2012, 2014b; Marley & Robinson 2015). Any substellar atmosphere model must be able to capture this behavior as it alters the atmospheric temperaturepressure profile and the boundary condition for thermal evolution.

Our radiative-convective equilibrium model solves for a hydrostatic and radiative-convective equilibrium temperature structure by starting with a first guess profile that is convective only in the greatest depths of the atmosphere and in radiative equilibrium elsewhere. Given this initial guess temperature profile and a radiative-convective boundary pressure, the model adjusts the temperature in the radiative regions using a straightforward Newton–Raphson scheme (see Marley & Robinson 2015) until the fractional difference between the net thermal flux and $\sigma T_{\rm eff}^{4-12}$ is everywhere less than a specified value, typically 10^{-5} .

Convective adjustment begins once a converged radiative profile has been found for a given specification of the top of the convection zone. The local temperature gradient $\nabla = d \log T /$ $d \log P$ is compared to that of an adiabat, $\nabla_{\rm ad}$ as tabulated employing the equation of state (Section 2.7). If the radiativeequilibrium lapse rate $\nabla_{\rm rad} > \nabla_{\rm ad}$ then that layer is deemed convective and ∇ is set equal to ∇_{ad} for that layer. Baraffe et al. (2002) have shown that for substellar, H₂-dominated atmospheres, convection is essentially adiabatic and that mixinglength theory predicts $\nabla = \nabla_{ad}$ in convective regions, regardless of the choice of the mixing length. Thus, for the cases studied here, setting $\nabla \equiv \nabla_{ad}$ in regions where $\nabla_{rad} > \nabla_{ad}$ is warranted. To find a properly converged structure, we specifically do not attempt to adjust the entire model region where $\nabla_{\rm rad} > \nabla_{\rm ad}$ to the adiabat all at once as changes in the deep temperature profile can and do impact the thermal energy balance and temperature profile above. Instead we re-compute a radiative-equilibrium solution for the new convection zone boundary and repeat the procedure. This iterative approach follows McKay et al. (1989) as adapted to giant planet and brown dwarf atmospheres by Marley et al. (1996, 1999) and Burrows et al. (1997).

The model employs 90 vertical layers which have 91 pressure–temperature boundaries or levels. The top model pressure is typically $\sim 10^{-4}\, \rm bar$ and the bottom pressure varies with model gravity and $T_{\rm eff}$, ranging from tens of bar to 1000

bar or more. The highest pressures are needed to capture the radiative-convective boundary in some high-gravity models. The line-broadening treatment, and thus the gas opacities, at such high pressures is very uncertain, which adds a source of uncertainty to the radiative-convective boundary location in such situations.

Once there is a converged solution for the top of the deepest convection zone, the radiative-equilibrium profile in the remainder of the atmosphere is compared to the local adiabat. Convective layers are inserted, one at a time, as necessary. Examples of converged radiative-convective equilbrium models with one, two, and three convection zones are shown in Figure 1 for a selection of model gravities and metallicities.

For most cases the lowermost radiative-convective boundary falls around 2000 K at which temperature the peak of the Planck function falls near the *H*-band spectral window in water opacity, permitting cooling to space. As expected from stellar atmosphere theory, the higher overall opacity of higher metallicity models shifts the entire structure to lower pressures for the same effective temperature and gravity.

2.3. Opacities

We consider the opacity of 20 molecules and five atoms (see Table 2). Details on how line widths are applied to a given line list and the opacity calculation in general are presented in Freedman et al. (2008, 2014) and Lupu et al. (2014). Since those publications we have updated several notable sources of opacity including H₂O, CH₄, the alkali metals, and FeH. Below we discuss our opacity sources for these species as well as our construction of opacity tables for use in the radiative-convective model and for the calculation of high-spectral-resolution spectra. We note that opacity line lists are constantly being updated and it is necessary to freeze the choice of line lists in order to produce a model set. Future versions of the Sonora models will include updated opacities as warranted.

2.3.1. Neutral Alkali Metals and Atoms

We use a new calculation of atomic line absorption from the neutral alkali metals (Li, Na, K, Rb, and Cs). These are now included using the VALD3 line list¹³ (Ryabchikova et al. 2015). Atomic line profiles, with the exception of the Na I and K I D lines, are assumed to be Voigt profiles without applying a line cutoff in strength or frequency. The line width is calculated from the Van der Waals broadening theory for collisions with H₂ molecules using the coefficient tabulated in the VALD3 database when available or from the codes of P. Barklem (https://github.com/barklem) otherwise. In all cases the classical Unsöld width (e.g., Kurucz & Avrett 1981) is corrected for a background gas of H2 and He rather than atomic H, accounting for the differences in polarization and reduced mass. The choice of line cutoff for the atomic species, with the exception of the D lines, has no material effect on the models.

The D resonance doublets of Na I (\sim 0.59 μ m) and K I (\sim 0.77 μ m) can become extremely strong in brown dwarf spectra and their line profiles can be detected as far as \sim 3000 cm⁻¹ from the line center in T dwarfs (Liebert et al. 2000; Burrows et al. 2000a; Marley et al. 2002). Under these circumstances, a

¹² For irradiated models, not considered here, the net thermal flux must also carry the net incident radiation absorbed below each atmospheric level.

¹³ http://vald.astro.univie.ac.at/~vald3/php/vald.php)

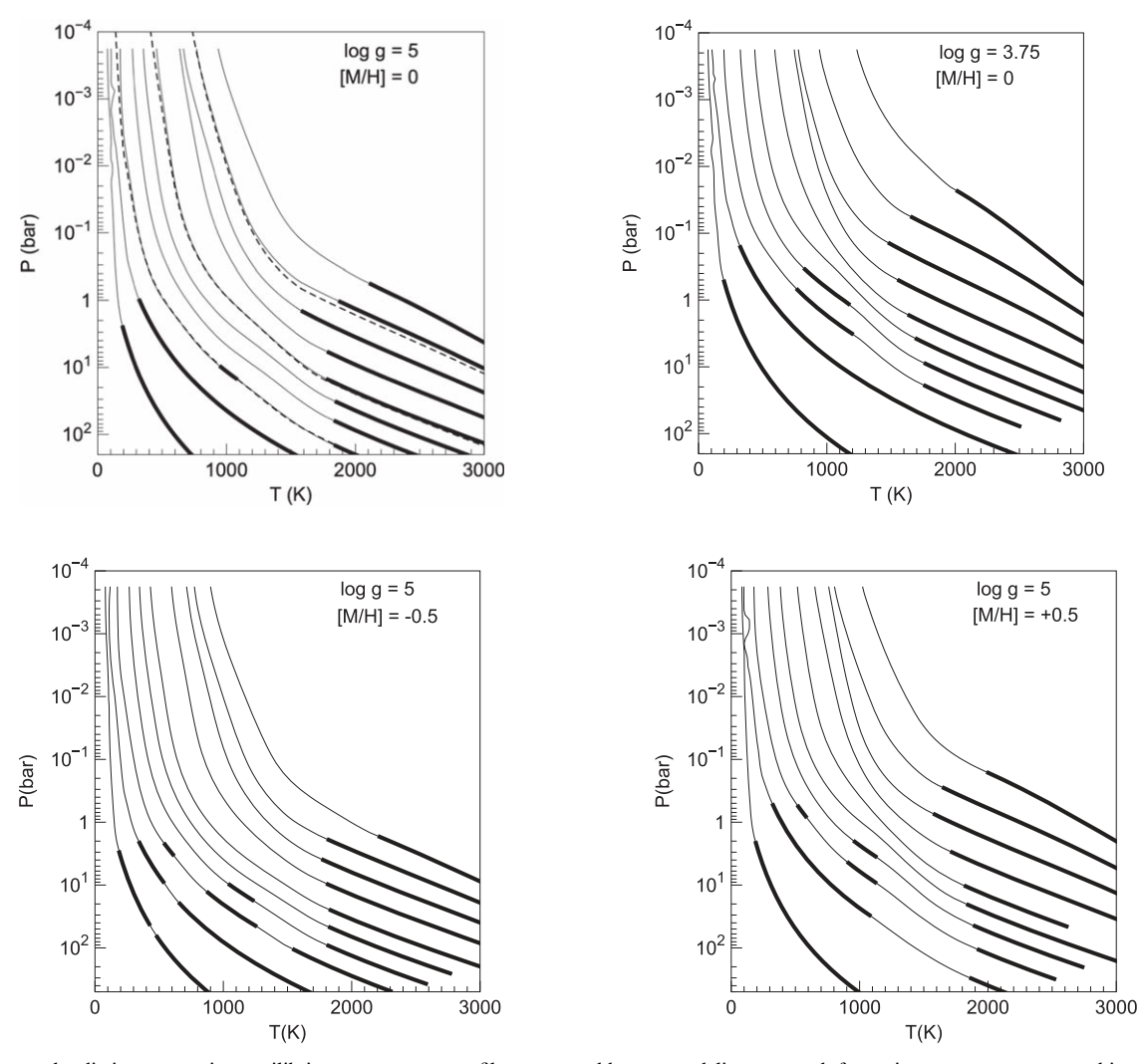


Figure 1. Converged radiative-convective equilibrium temperature profiles computed by our modeling approach for various parameters as noted in each panel. In all panels, models are shown every 200 K from $T_{\rm eff} = 200$ to 1200 K and then every 300–2400 K. Thick lines show convective regions of the atmospheres. Note how at higher effective temperatures the boundary lies near 2000 K, then with falling $T_{\rm eff}$, convection turns on in some portions of the radiative region, until finally these isolated zones merge and the boundary moves up to near 1 bar in the coolest models. Dashed curves show cloudless, chemical equilibrium profiles from Phillips et al. (2020) for $\log g = 5$ and $T_{\rm eff} = 600$, 1200, and 2100 K.

Lorentzian line profile becomes grossly inadequate in the line wings and a detailed calculation is required.

For these two doublets, we have implemented line-wing profiles based on the unified line-shape theory (Rossi & Pascale 1985; Allard et al. 2007a, 2007b). The tabulated profiles (N. Allard 2000, private communication) are calculated for the D1 and D2 lines of Na I and K I broadened by collisions with $\rm H_2$ and He, for temperatures ranging between 500 and 3000 K and at a reference perturber ($\rm H_2$ or He) number density of $n_{\rm pert} = 10^{19}$ (K–H₂ profiles) or 10^{20} cm⁻³ (Na–H₂, Na–He and K–He profiles). Two collisional geometries are considered for broadening by $\rm H_2$ and averaged to obtain the final profile. The line core is described with a symmetric Lorentz profile with a width calculated from the same theory, with coefficients given in Allard et al. (2007b).

The line profiles are provided as a set of coefficients in a density expansion that allows their evaluation at a range of densities other than the reference density of the tabulation. The third-order expansion is considered suitable up to perturber densities of $10^{20} \, \mathrm{cm}^{-3}$ (N. Allard, private communication) and the Lorentzian line width is linear in perturber density

(Allard et al. 2016). Using those expressions and by interpolating in temperature, we produce a set of profiles covering 500–3000 K and $15 \le \log n_{\rm pert} \le 20$ on a uniform grid. In atmosphere models and spectra that may exceed these limits, we refrain from extrapolating. This is generally acceptable since the Na I and K I resonance doublets play a lesser role in the total opacity outside of these boundaries. Nonetheless, calculations that reach higher densities are valuable. After the models presented here were computed, Allard and collaborators presented new tables for K–H₂ (Allard et al. 2016) and Na–H₂ (Allard et al. 2019) valid to higher pressure. We will use those tables in future updates to the model grid. Tests show that while the new treatment does impact the model spectral slope near 1 μ m, it does not appreciably alter the temperature profiles from the present model generation.

2.3.2. FeH

For FeH we use the line list of Dulick et al. (2003) which was our opacity source in previous models. However, this list did not include the E-A band at $1.6\,\mu m$ which is prominent in M and L dwarfs. Here we include this rovibrational

Table 2
Molecular Opacity Sources

Molecule	Opacity Source(s) ^a	Line Widths ^b
C_2H_2	H12	W16
C_2H_4	H12	air
C_2H_6	H12	air
CH ₄	Yurchenko et al. (2013), Yurchenko & Tennyson (2014) d, ¹³ CH ₄ STDS	P92
CO	HT10; isotopologues Li et al. (2015)	L15
CO_2	Huang et al. (2014)	scale
CrH	Burrows et al. (2002)	lin.
FeH	Dulick et al. (2003); Hargreaves et al. (2010)	lin.
H_2O	Tennyson & Yurchenko (2018); isotopologues	UCL
	(HDO not included) Barber et al. (2006)	
H_2S	ExoMol ^d ; Azzam et al. (2015);	K02
	isotopologues H12	
HCN	Harris et al. (2006); Harris et al. (2008);	lin.
	isotopologues GEISA ^f	
LiCl	Weck et al. (2004) ^c	lin.
MgH	Weck et al. (2003) ^c	lin.
N_2	H12	air
NH_3	Yurchenko et al. (2011)	W16
OCS	H12	W16
PH_3	Sousa-Silva et al. (2015) ^d	S04
SiO	Barton et al. (2013); Kurucz (2011) ^f	lin.
TiO	Schwenke (1998); Allard et al. (2000)	lin.
VO	McKemmish et al. (2016); ExoMol	lin.

Notes.

 $E^4\Pi_i - A^4\Pi_i$ electronic transition, employing a line list from Hargreaves et al. (2010). This list was constructed by fitting to empirical spectra of cool M dwarfs and to laboratory measurements. As a consequence there are multiple uncertainties in the line list, including the lower energy level of many of the lines, which are set to a constant value. Hargreaves et al. (2010) ultimately applied an enhancement factor of 2.5 to their initial line strengths in stellar-atmosphere models in order to match observations. In our own initial test models employing this line list we found that the predicted band strength as seen in our models was far in excess of that observed in early L dwarfs. After discussions with R. J. Hargreaves (2015, private communication) on various sources of uncertainty we decided to reduce the line strengths for this band only by a factor of 1/3, slightly overcorrecting to remove the correction factor of 2.5 to better match observations. This is the only absorption band in our entire model set for which we have applied such an empirical correction.

2.3.3. Line Profiles

The proper choice of line widths to apply to each individual molecular line is a difficult problem as there is often little to no theoretical or laboratory guidance, particularly for higher quantum number transitions that are important at higher temperatures. For each molecule we have applied the best information available at the time our opacity database was constructed although in many cases we have had to estimate the broadening with limited information. Table 2 summarizes our choices for line widths, including cases in which we used literature values or widths appropriate to air, rather than H_2 —He mixtures.

In most molecular line lists, the maximum J quantum number is above 100. However, Lorentz broadening coefficients are typically only available up to $J \sim 50$, which we term J_{low} . In such cases where data are lacking, we extrapolate the broadening parameter γ by assuming a value, $\sim 0.075 \, \text{cm}^{-1} \, \text{atm}^{-1}$, for the lowest J value in any set then adjusting the broadening at any J by a linear expression in $J - J_{\text{low}}$ up to some maximum J. Above that J, γ is held fixed at $\sim 0.04 \, \text{cm}^{-1} \, \text{atm}^{-1}$. A similar approach has been followed by the UCL group (J. Tennyson 2018, private communication).

2.3.4. Opacity Tables

Opacities are computed at each of 1060 distinct pressure-temperature points covering the range $75 \leqslant T \leqslant 4000 \, \mathrm{K}$ and $10^{-6} \leqslant P \leqslant 300 \, \mathrm{bar}$ on a wavenumber grid constructed such that there are about 3 points per Doppler width for the H_2O molecule. This typically amounts to roughly 2×10^6 individual points for intermediate T and P with up to 10^7 points at the lowest pressures at which we compute the opacity from up to 10^{10} individual spectral lines (for example, in the case of CH_4). This tabulated opacity is used both in post-processing to construct high-resolution spectra for individual models and also to compute k coefficients which are used to calculate the atmospheric structure.

To calculate the k coefficient we sum the contribution of every molecule to the total molecular opacity by weighting by their relative equilibrium abundances (see next section). Within each of 190 spectral bins covering the wavelength range 0.4 to 320 μ m, we then compute the k coefficients using the summed opacity. We note that this is more accurate than later combining k coefficients computed for individual gases (e.g., Lacis & Oinas 1991; Amundsen et al. 2017). This approach, however, removes flexibility in adjusting local gaseous mixing ratios, for example, to account for disequilibrium chemistry effects (see Amundsen et al. 2017 for a recent discussion). We use 8 Gauss points for the k coefficients, following a double Gaussian scheme in which 4 points cover the range 0 to 0.95 of the cumulative distribution and 4 additional points cover the range 0.95 to 1.00. This permits more precise resolution of the strongest few percent of the molecular lines within any given spectral bin. Tests (M. Line 2020, private communciation) have shown that this double-Gauss approach yields essentially identical thermal profiles as those computed with 20 Gauss points covering the full distribution range of 0 to 1.0 and the same opacities. The k coefficients for all of the model cases presented here are available for download here.

In addition to these opacity sources we also account for several other continuum opacity sources. Pressure-induced opacity from H_2 – H_2 , H_2 –H, H_2 –He, H_2 – N_2 , and H_2 – CH_4 is accounted for as described in Saumon et al. (2012). We also include bound–free and free–free opacity from H^- and H_2^+ and free–free opacity from H_2^- and H_2^- as well as electron scattering. Rayleigh scattering from H_2 , H, and He is also included. We note in passing that, despite the recent "discovery" of the importance of H^- opacity in

^a H12 = HITRAN 2012 (Rothman et al. 2013); http://www.cfa.harvard.edu/hitran/updates.html; HT10 = HITEMP 2010 (Rothman et al. 2010); http://www.cfa.harvard.edu/hitran/HITEMP.html .

^b lin. = linear estimate for γ , see text; air = air widths from H12; scale = 1.85 × self broadening; K02 = Kissel et al. (2002); L15 = Li et al. (2015); P92 = Pine (1992); S04 = Salem et al. (2004); W16 = Wilzewski et al. (2016); UCL = ExoMol web page^d.

^c http://www.physast.uga.edu/ugamop/.

d http://www.exomol.com (Tennyson & Yurchenko 2012).

e http://ether.ipsl.jussieu.fr/etherTypo/?id=950.

f http://kurucz.harvard.edu/molecules.html.

transiting planet atmospheres¹⁴, H⁻ has long been recognized as an important source of continuum opacity in cool stars (Chandrasekhar & Münch 1946). Our models have always included this opacity source since Marley et al. (1996). The models in this paper do not include cloud opacity; our method for accounting for such opacity will be presented in a future paper in the series.

2.4. Radiative Transfer

In the radiative-convective model we compute radiative fluxes through each model layer using the "two-stream source function method" outlined in Toon et al. (1989). This scheme first computes a two-stream (up and down) solution to the flux and then uses the two-stream solution as the source function for scattering in the second calculation step that computes the flux in six discrete beams. Following Toon et al., within each model layer n, with optical depth ranging from $\tau = 0$ at the top to $\tau = \tau_{bot}$ at the bottom, the source function is linearized as $B_n(\tau) = B_{0n} + B_{1n}\tau$ where B_{0n} is the Planck function at the temperature at the top of the layer and $B_{1n} = [B(T(\tau_{bot})) + B_{0n}]/\tau_n$. The final upward and downward fluxes are computed by integration over the multiple streams. The method is exact for pure absorption and provides an acceptable balance between accuracy and speed for cases with particle scattering. Toon et al. (1989) provide tables of the size of the error in various cases. The lower and upper boundary conditions are those commonly used in the stellar atmospheres problem for semi-infinite atmospheres (Hubeny & Mihalas 2014). Recently, Heng & Kitzmann (2017) have extended the Toon et al. method for greater accuracy in strongly scattering atmospheres, a limit we do not reach in the cloudless models presented here.

Once we have a converged T(P) model we compute high-resolution spectra by solving the radiative transfer equation for nearly 362,000 monochromatic frequency points between 0.4 and 50 μ m. The monochromatic opacities are calculated from the same opacity database, line broadening, and chemistry tables as the k coefficients and are pre-tabulated on the same (T, P) grid. In these cloudless models, the radiative transfer equation is solved with the Rybicky solution (Hubeny & Mihalas 2014) assuming that Rayleigh scattering is isotropic. The resulting spectral energy distributions are in excellent agreement with those obtained from the lower-resolution k-coefficient method with their respective integrated fluxes differing by less than 2% in nearly all cases.

2.5. Chemical Equilibrium

Chemical equilibrium abundances at the grid (*P*, *T*) points were calculated using a modified version of the NASA CEA Gibbs minimization code (see Gordon & McBride 1994) based upon prior thermochemical models of substellar atmospheres (Fegley & Lodders 1994, 1996; Lodders 1999, 2002; Lodders & Fegley 2002; Visscher et al. 2006, 2010; Visscher 2012) and recently used to explore gas and condensate chemistry over a range of atmospheric conditions (Morley et al. 2012, 2013; Moses et al. 2013; Kataria et al. 2016; Skemer et al. 2016; Burningham et al. 2017; Wakeford et al. 2017).

Equilibrium abundances (with a focus on key constituents that are included in the opacity calculations: H_2 , H, H^+ , H^- , H_2^- , H_2^+ , H_3^+ , H_2^- , H_2^+ , H_3^+ , H_2^- , H_3^+ , H_2^- , H_3^+ , H_3^-

 C_2H_4 , C_2H_6 , NH_3 , N_2 , PH_3 , H_2S , SiO, TiO, VO, Fe, FeH, MgH, CrH, Na, K, Rb, Cs, Li, LiOH, LiH, LiCl, and e⁻) were calculated over a wide range of atmospheric pressures (1 μ bar to 300 bar) and temperatures (75 to 4000 K) and over a range of metallicities (-1.0 dex to +2.0 dex relative to solar abundances, assuming uniform heavy-element enrichment), and C/O element abundance ratios (0.25 to 2.5 times the solar C/O abundance ratio of C/O = 0.458) using protosolar abundances from Lodders (2010) which represent the bulk solar system composition and provide continuity with earlier iterations of the chemical models. Other C/O ratios can be adopted (e.g., $1.25 \times C/O$, corresponding to C/O = 0.57) for consistency with more recent determinations of the photospheric C/O ratio (e.g., Asplund et al. 2009; Caffau et al. 2011; Lodders 2020; Asplund et al. 2021).

For a given metallicity, variations in the C/O ratio were computed while holding the C+O abundance constant, so that the total heavy-element abundance relative to hydrogen (Z/X), characterized by [M/H], remains constant. For example, to achieve C/O ratios greater than the solar value (e.g., $1.25 \times$ or $1.5 \times$ the adopted solar ratio of C/O = 0.458), the oxygen abundance is slightly diminished while the carbon abundance is slightly enhanced. For most species, we utilized the thermochemical data of Chase (1998) with additional thermochemical data from Gurvich et al. (1989, 1991, 1994), Burcat & Ruscic (2005), and Robie & Hemingway (1995) for several mineral phases.

Condensation from the gas phase is included with the "rainout" approach of Lodders & Fegley, wherein condensates are removed from the gas mixture lying above the condensation level. This prevents further gas-condensate chemical reactions from occurring higher up in the atmosphere, above the condensation point. Rainout has been validated for alkali species by the sequence of the disappearance of Na and K spectral features (Marley et al. 2002; Line et al. 2017; Zalesky et al. 2019).

As in previous thermochemical models, the equilibrium abundance of any condensate-forming species at higher altitudes is determined by its vapor pressure above the condensate cloud (Visscher et al. 2010). The detailed equilibria models of Lodders (2002) show that several elements (such as Ca, Al, Ti) may be distributed over a number of different condensed phases depending upon pressure and temperature conditions. For simplicity, here we consider the vapor pressure behavior of TiO and VO in equilibrium with Ti₂O₃, Ti₃O₅, or Ti₄O₇, and V₂O₃, V₂O₄, and V₂O₅, respectively, as we are primarily interested in the behavior of Ti and V above the cloud deck and the current grid lacks the resolution for detailed Ca-Ti equilibria as a function of temperature. The behavior of Mg-, Si-, and Fe-bearing gases was calculated following the approach of Visscher et al. (2010) and included the equilibrium condensation of forsterite (MgSiO₄), enstatite (MgSiO₃), and Fe metal. As in Lodders (1999), major condensates for the alkali elements included LiCl, LiF, Na2S (see also Visscher et al. 2006), KCl (see also Morley et al. 2012) RbCl, and CsCl.

2.6. Comparison to Other Approaches

As mentioned above, the construction of any forward model involves numerous choices and trade-offs. When comparing models from different groups, it is worth keeping in mind the various approximations and assumptions behind the models. Here we highlight a few such differences.

 $^{^{14}}$ E.g., Arcangeli et al. (2018) proposed H $^-$ and H $_2$ O dissociation as the natural, expected solution to explain Ultra-Hot Jupiter spectra, as earlier studies neglected to include this opacity source.

Our modeling scheme, with roots in solar system atmospheres, was first applied to a brown dwarf (Gl 229 B) in Marley et al. (1996). That same year, Allard et al. (1996) likewise applied the PHOENIX modeling scheme, with roots in stellar atmospheres, to the same object. Both models developed over time with the PHOENIX model ultimately producing the widely cited COND and DUSTY model sets (Allard et al. 2001). In contrast to our approach of using pre-tabulated chemistry and opacities, the PHOENIX model computes chemistry and opacities on the fly. COND also employs full equilibrium chemistry rather than rainout chemistry to compute molecular abundances. As we note above, recent retrieval studies have validated rainout chemistry in the context of T dwarfs. To compute fluxes, PHOENIX uses the sampling method in which the radiative transfer is only computed at a finite number ($\sim 10^5$ or more, T. Barman 2017, private communication) of wavelength points. Our method accounts for the opacity and uses the information at many more (10^6-10^7) points, but only in a statistical sense as the opacity distribution within wavelength bins is described by k coefficients.

A more recent version of the PHOENIX model is known as BT-Settl (Allard et al. 2014), where the BT denotes the source of the water opacity employed (Barber et al. 2006) and the Settl denotes the handling of condensate opacity. These models have not been as thoroughly described and a more detailed comparison is not yet possible.

Recent studies of radiative transfer for transiting planets have found that the *k*-coefficient method more closely reproduces calculations performed at very high spectral resolution that the sampling method, since the entire range of both low- and high-opacity wavelengths is considered (Garland & Irwin 2019). In practice, for most of the atmospheres considered here, this is unlikely to be a major difference. However, our own tests of fluxes computed with opacity sampling find that at low temperatures, where there are relatively few opacity sources and the opacity can vary wildly with wavelength, sampling can produce large errors unless many more points are employed than typically used. A systematic comparison between the approaches would be informative. Differences between the approaches in the context of cloud opacity will be discussed in a future paper.

Another widely cited model set is that of the Adam Burrows's group which consists of two different approaches. The models presented in Burrows et al. (1997, 2001) were computed using the Marley et al. (1996, 1999) radiative-convective model described above. After 2001 the Burrows group transitioned to a modeling framework based on a widely used stellar atmospheres code TLUSTY (Hubeny 1988; Hubeny & Lanz 1995) adapted for use in brown dwarfs (e.g., Burrows et al. 2002, 2004, 2006). This work uses the sampling method to handle opacities, like PHOENIX, but with the ability to handle rainout and quenching (Hubeny & Burrows 2007) rather than relying on pure equilibrium chemistry. There are also differences in the treatment of radiative transfer and the global numerical method used to solve the set of structural equations. Hubeny (2017) provides a thorough, critical comparison of various approaches employed in substellar models.

Recently Malik et al. (2017) released the open-source atmosphere radiative-equilibrium modeling framework HELIOS. As of this date the model structures are strictly in radiative equilibrium. HELIOS computes atmospheric structure assuming true chemical equilibrium, not rainout chemistry, using a fast analytic approximation of the C, N, O chemistry (Heng et al. 2016). The model

uses k coefficients of individual molecules which they combine on the fly using "random overlap" approximation rather than the premixed opacity tables employed here or the "re-bin and re-sort" method usually used to combine k coefficients (see Amundsen et al. 2017). While fast, this approximation can produce large flux errors in certain cases because, in fact, the opacities are not random but are vertically correlated through the atmosphere (Amundsen et al. 2017). There has not yet been a systematic comparison of model atmospheres computed by HELIOS with other models using more traditional methods for computing non-irradiated substellar atmospheres.

As noted in Section 1, the model set most similar to our own is Phillips et al. (2020). Those authors made generally similar modeling choices, including rainout equilibrium, although for the opacities, they mix single-gas k coefficients following Amundsen et al. (2017) rather than pre-computing them for the mixture, as we do here. They do not discuss whether their models produce multiple layer convection zones, although it appears from their posted structures that they in fact do, with generally similar structure as our Figure 4. Their models are only for solar metallicity and those authors advise users to only trust models below $T_{\rm eff} = 2000 \, \text{K}$, despite the grid going to higher temperatures as they neglect some important opacity sources. Where they can be compared, the Phillips T(P) profiles are very similar to our own, as seen in Figure 1, except above 2000 K where they are slightly cooler, as expected given their neglect of some opacities.

When comparing atmospheric abundances computed by our approach and other methods it is crucial to consider the impact of our rainout chemistry assumption (see, e.g., Lodders & Fegley 2006). Because of rainout, certain species that can potentially be significant sinks of atoms of interest, do not form. For example, under rainout conditions, Fe₂O₃, does not form as the Fe condensate is removed from the atmosphere. Rainout atmospheres cooler than the iron oxide condensation temperature will thus appear to have larger O abundances than other treatments with the same initial O abundance. Likewise, rainout causes the removal of condensed aluminum oxide Al₂O₃ from the atmosphere, preventing the formation of albite (NaAlSi₃O₈) which would otherwise remove atomic sodium from the atmosphere at about 1000 K. Retrieval studies have shown (Zalesky et al. 2019) that the rainout chemistry prediction is most consistent with the observed spectra of T dwarfs.

The rainout chemical equilibrium abundance tables used to compute the models presented here are available along with the models at our model page. 15

2.7. Evolution Model

The model for the interior and the evolution is discussed in detail in Saumon & Marley (2008; hereafter, SM08). Briefly, the interior is modeled as fully convective and adiabatic and uses the atmosphere models described herein as the surface boundary condition. We generate sequences for the three metallicities of the atmosphere models ([M/H] = -0.5, 0 and 0.5). The models are started with a large initial entropy ("hot start") and include fusion of the initial deuterium content.

We incorporate three significant improvements over the models of SM08. First, we now account for metals in the equation of state by using an effective helium mass fraction

¹⁵ https://doi.org/10.5281/zenodo.5063476

(Chabrier & Baraffe 1997)

$$Y' = Y + Z \tag{1}$$

where Y = 0.2735 is the primordial He mass fraction and Z the mass fraction of metals (Z = 0.00484, 0.0153 and 0.0484, corresponding to [M/H] = -0.5, 0, and +0.5, respectively). The hydrogen and helium equations of state are from the tables of Saumon et al. (1995), as in SM08. Second, we use the improved nuclear-reaction screening factors of Potekhin & Chabrier (2012). Third, the new surface boundary condition is provided by the atmospheres presented here which are defined over a finer ($T_{\rm eff}$, $\log g$) mesh and extend to lower gravity ($\log g = 3$) and lower $T_{\rm eff} = 200$ K. This allows modeling of lower mass objects, down to $0.5 M_{\rm L}$

2.8. Previous Applications

Our group has applied the same basic modeling approach described here to a number of topics related to ultracool dwarfs and extrasolar giant planets. This work is generally summarized in Marley & Robinson (2015). Notable applications have included computation of the evolution tracks presented in Burrows et al. (1997), characterization of L and T dwarfs from their near-infrared spectra in Cushing et al. (2008) and Stephens et al. (2009), calculation of atmospheric thermal profiles of irradiated giant planets (Fortney et al. 2005), and modeling of young directly imaged planets in (Marley et al. 2012). Our prediction that the clearing of clouds at the L/T transition would result in an excess of transition brown dwarfs (Saumon & Marley 2008) was recently validated with the 20 pc brown dwarf census of Kirkpatrick et al. (2021).

In addition, Fortney et al. (2008) investigated the atmospheric structure and spectra of cloud-free gas giants from 1–10 Jupiter masses, for models with $T_{\rm eff}$ < 1400 K. The role of enhanced atmospheric metallicity, an outcome expected from the core-accretion model of planet formation (e.g., Fortney et al. 2013), was investigated as a way to observationally distinguish planets from stellar-composition brown dwarfs. These atmosphere models were coupled to the "cold start" and "hot start" evolutionary tracks of Marley et al. (2007) to better understand the magnitudes and detectability of young giant planets. Later, Fortney et al. (2011) modeled the evolution of the atmospheres of the solar system's giant planets to investigate how metal enrichment and the timevarying (but modest) insolation effect our understanding of the cooling history of these planets.

While earlier models included the iron and silicate clouds that form in L-dwarf atmospheres, Morley et al. (2012) considered the salt and sulfide clouds (Visscher et al. 2006) that likely form in cooler T-dwarf atmospheres, finding that models that included the formation of these additional species could better match the colors of the T-dwarf population. Morley et al. (2014b) focused on even colder objects, the Y dwarfs, many of which are cold enough to condense volatiles like water into ice clouds. Morley et al. (2014a) considered how either clouds or hot spots could cause wavelength-dependent variability in T- and Y-dwarf spectra.

3. Model Results

3.1. Thermal and Composition Profiles

Radiative-convective equilibrium thermal profiles are shown for a selection of model parameters in Figure 1 for two gravities at solar metallicity and two metallicities at fixed gravity. The general behavior of the extent of the convection zones apparent in previous work is also seen here. At the highest effective temperatures the single radiative-convective boundary lies near 2000 K and at pressures in the range of 1–0.01 bar, depending on gravity. As the effective temperature falls the top of this convection zone stays near 2000 K but moves to progressively higher pressures. Finally, for effective temperatures below 1000K, the denser regions of the atmosphere begin to be cooler than about 1000 K, resulting in the peak of the local Planck function lying not in the relatively clear, low-opacity regions from 1 to 2 μ m but rather in the higher gas opacity region between 2 and 4 μ m. Consequently, a second detached convection zone forms around 1000 K.

The second transition from convective to radiative transport occurs when sufficient flux can emerge through the spectral window at 4 to 5 μ m. In some cases a third, small convection zone briefly develops higher in the atmosphere. Finally, with falling effective temperature, these detached zones merge and the atmosphere is finally fully, or almost fully, convective all the way up to about 0.1 to 1 bar, depending on gravity. The universality of \sim 0.1 bar radiative-convective boundaries at low $T_{\rm eff}$ and g has been explored by Robinson & Catling (2014).

Correctly mapping the detached convection zones is important for the evolution calculation as they change the atmospheric temperature gradient away from that of pure radiative equilibrium. This in turn alters the temperature and pressure—and thus atmospheric entropy—of the deep radiative-convective boundary, which ultimately controls the thermal evolution of the entire object.

Likewise, this behavior of the radiative regions rapidly merging, raising the radiative-convective boundary to pressures near 1 bar at cooler effective temperatures is likely the explanation for the rapid rise in the eddy-mixing coefficient, as inferred from observed disequilibrium chemistry below 400 K (Miles et al. 2020).

3.2. Model Spectra

All of the model spectra described in this paper are available online. ¹⁶ Here we briefly describe the characteristics of the model set.

Spectra for a selection of model cases and wavelength ranges are shown in Figures 2 through 7. While these cloudless models are of course less relevant to observed spectra through much of the L-dwarf regime, they are nevertheless instructive for illustrating how the atmospheric chemistry evolves as effective temperature falls through the M, L, T, and Y spectral types.

As the atmosphere cools, molecular features become more prominent and the roughly blackbody spectra apparent at 2400 K is nearly unrecognizable by 400 K (Figure 2). The universality of the M-band flux excess, first noted in Marley et al. (1996), is apparent as are the familiar excesses in Y, J, H, and K bands. All of these arise from opacity windows allowing flux to escape from deep-seated regions of the atmospheres where the local temperature often exceeds $T_{\rm eff}$. The folly, for most purposes, of attempting to describe the thermal emission of brown dwarfs or self-luminous planets as being blackbody-like is evident from casual inspection of Figure 2.

¹⁶ https://doi.org/10.5281/zenodo.5063476

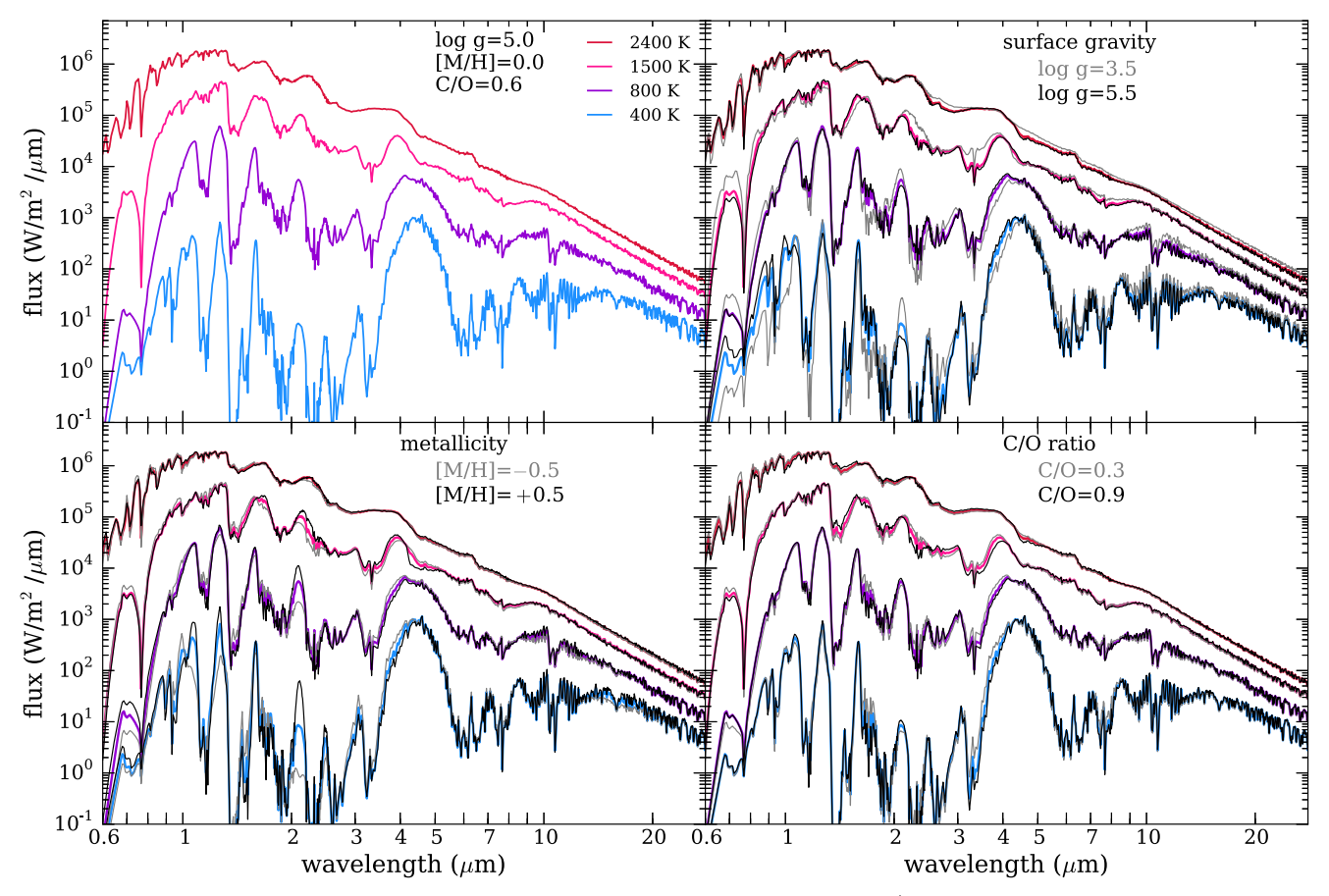


Figure 2. Overview of complete model spectra for various combinations of surface gravity, metallicity, and C/O ratio. The line color labels the effective temperature as shown in the upper left panel. Spectral resolution R varies across the figure for clarity. Effective temperatures are as labeled in the top left panel. Models shown in the top left panel are repeated in the other three panels along with two variations (in gravity, metallicity, and C/O ratio) in black and gray, as labeled in each sub-panel. Of particular interest is the effect of metallicity on K-band emission (Fortney et al. 2008).

Spectral sequences for limited spectral ranges are shown in Figures 3 through 7. The red optical (Figure 3) is primarily sculpted by the K I resonance doublet centered around 0.77 μm (Burrows et al. 2000b). Because this spectral region otherwise has low gas opacity, the influence of the K absorption lingers in these cloudless models well below the $T_{\rm eff}$ at which potassium condensates form (around 700 K). Including the effects of the Na and K condensates changes the opacity as shown by Morley et al. (2012), but in the present cloudless models deep-seated K still influences the spectra down to $T_{\rm eff} \sim 400$ K. Finally, at the lowest effective temperatures, the signatures of water and methane appear, strikingly altering the predicted optical spectra redward of 0.80 μm .

Figure 4 depicts the crucial near-infrared region. With falling $T_{\rm eff}$ the familiar gradual departure of the refratory species and the alkalis, as well as the appearance of methane are apparent. The cloudless models are cooler than models that account for condensate opacity, thus methane appears around $T_{\rm eff}=1600~{\rm K}$ in H band, which is warmer than it is seen in nature (Kirkpatrick 2005). The progressive loss of flux in the K band, attributable to the increasing influence of pressure-induced opacity of molecular hydrogen, continues through the entire sequence. The flux peaks are progressively squeezed between stronger and stronger molecular absorption until, by 300 K, they become sharp and well separated. As in the previous figure, the coldest model shown, at 300 K, has a notably different morphology as ammonia features are

apparent near 1 μ m. This interesting small spectral region is further expanded in Figure 5.

The wavelength range to be explored in fresh detail by the James Webb Space Telescope beyond 3 μ m is explored in Figures 6 and 7. This is a region broadly sculpted by water opacity with important contributions from methane and ammonia at lower effective temperature. The 5 μ m spectral window allows deep-seated flux to emerge, as in familiar images of Jupiter (e.g., Orton et al. 1996). The long path lengths through the atmosphere, as in the near-infrared, permit detection of rare molecules (Morley et al. 2019). Gharib-Nezhad et al. (2021) consider the detectability of lithium-bearing molecules in this region.

Figure 8 explores the influence of the C/O ratio in the near-infrared among the coolest models where differences in methane abundance are most notable. Although these are pure chemical equilibrium models, the influence of disequilibrium chemistry is less notable in this spectral region at these cool effective temperatures, thus providing better tracers of the atmospheric C/O ratio, with the usual caveat of accounting for loss of O into condensates at higher temperatures.

Finally 9 compares the model spectra presented here to our earlier generation of models (Saumon et al. 2012) through the effective temperature range of the T and Y dwarfs. The most notable differences arise from changes in the alkali D line treatment and updated ammonia and methane opacity (Section 2.3). We have found that more recent updates to the

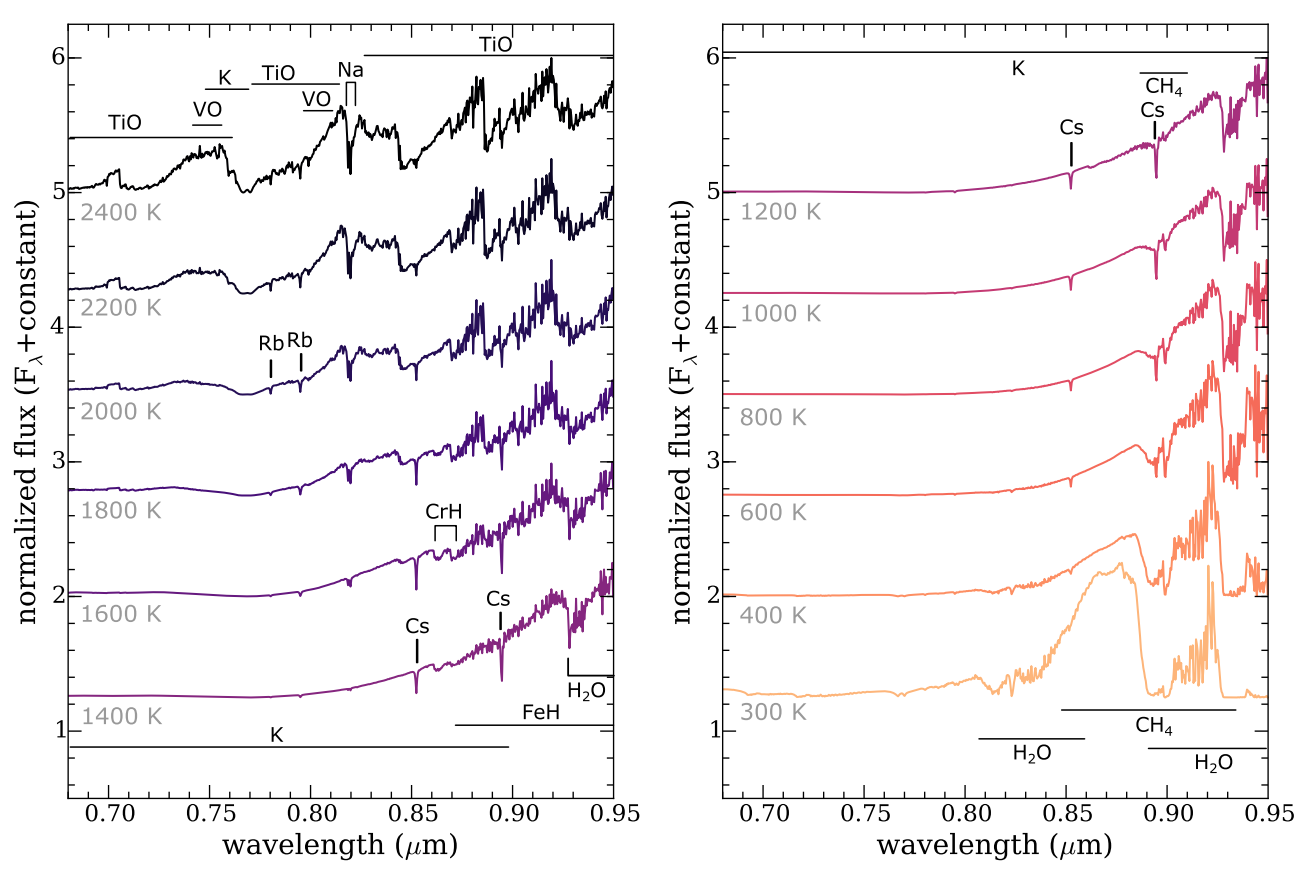


Figure 3. Red optical spectral sequence ($R \sim 2000$) of models for solar metallicity and C/O ratio at $\log g = 5$, shifted vertically for clarity. Notable absorption features are labeled.

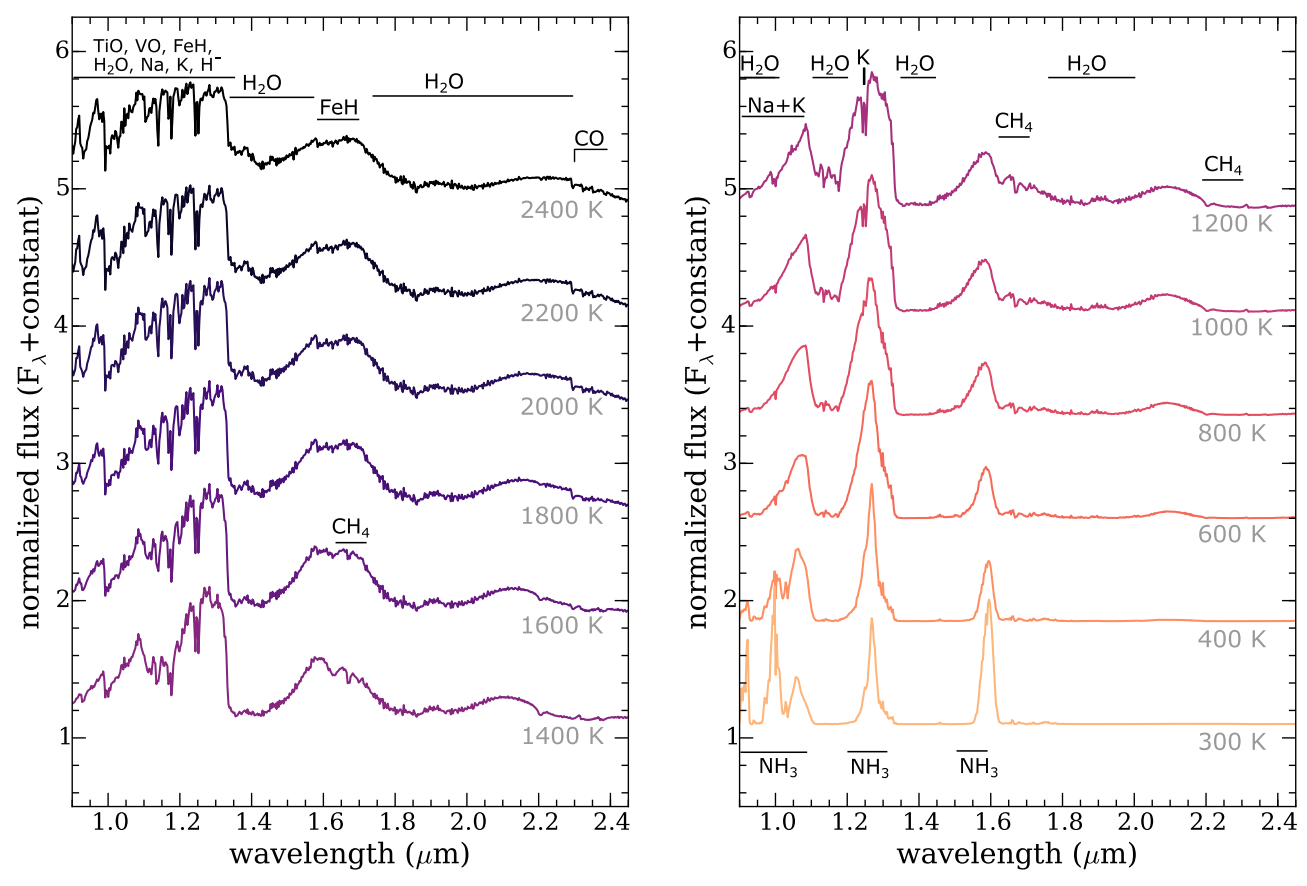


Figure 4. Same as Figure 3, but for far-red through near-IR spectral range with $R \sim 600$.

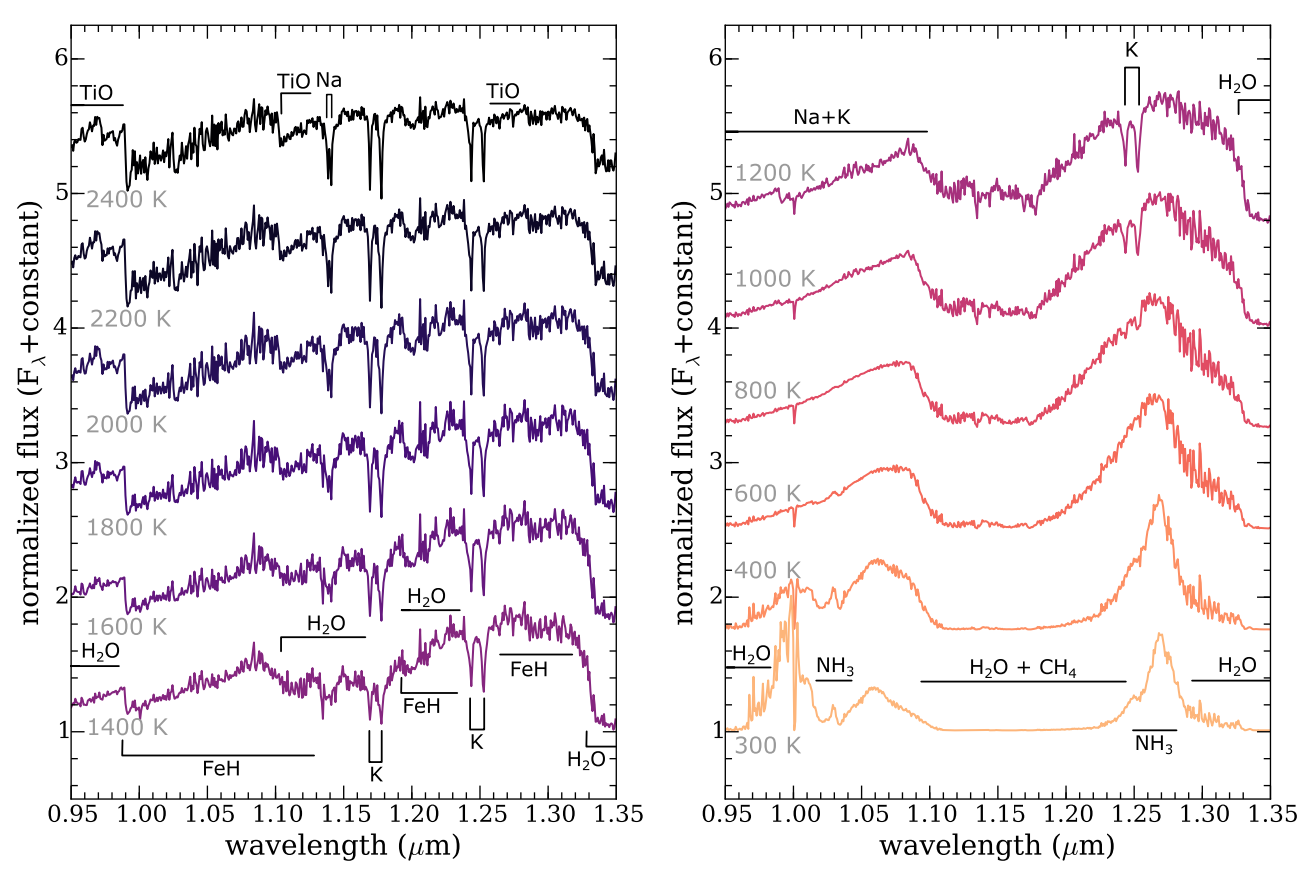


Figure 5. Same as Figure 3, but highlighting the spectral region near 1 μ m with $R \sim 1500$. In the coldest models, the loss of almost all major gaseous absorbers, particularly the alkali metals, except H₂O, NH₃, and CH₄, transforms the appearance of this spectral region.

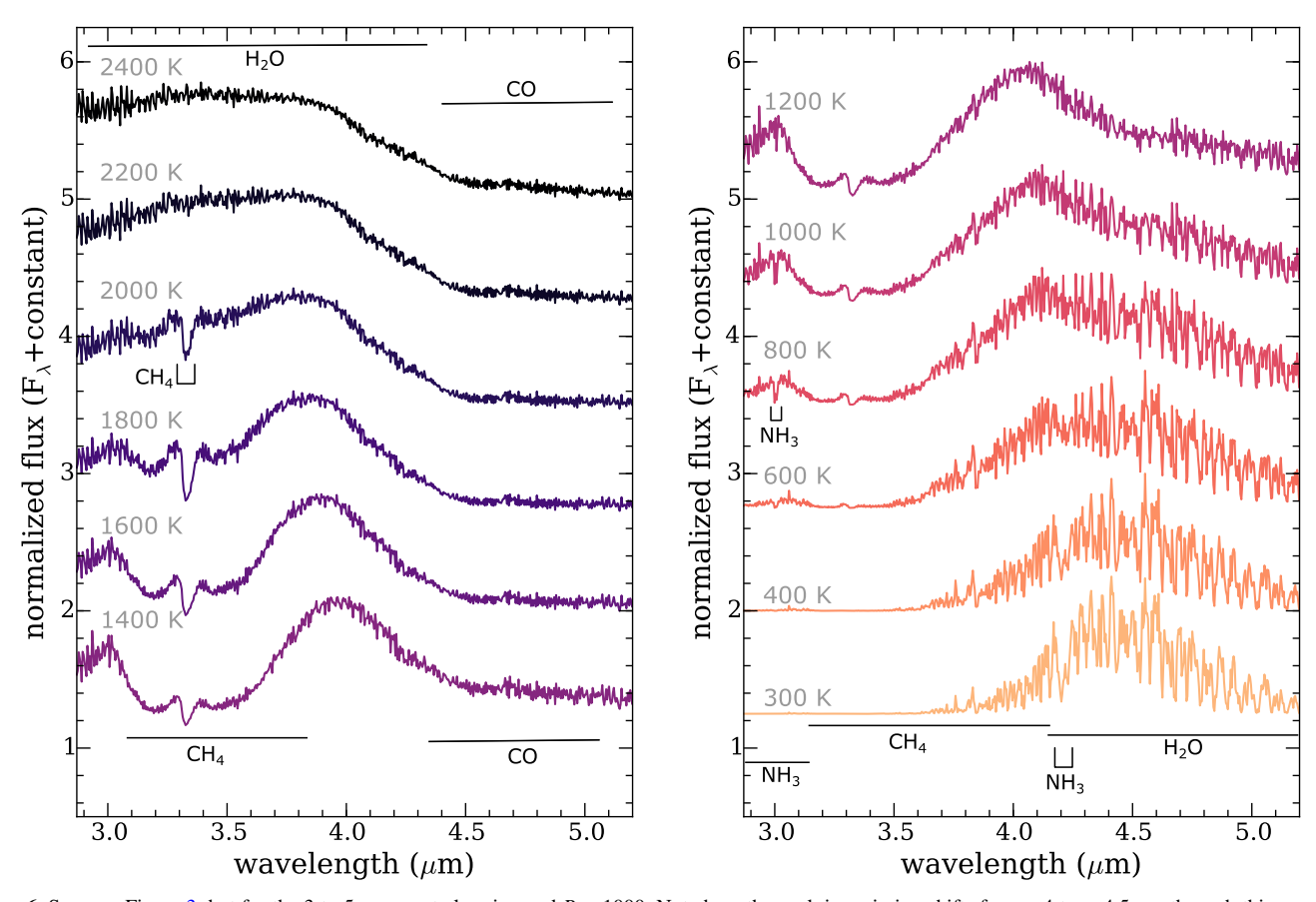


Figure 6. Same as Figure 3, but for the 3 to 5 μ m spectral region and $R \sim 1000$. Note how the peak in emission shifts from \sim 4 to \sim 4.5 μ m through this sequence.

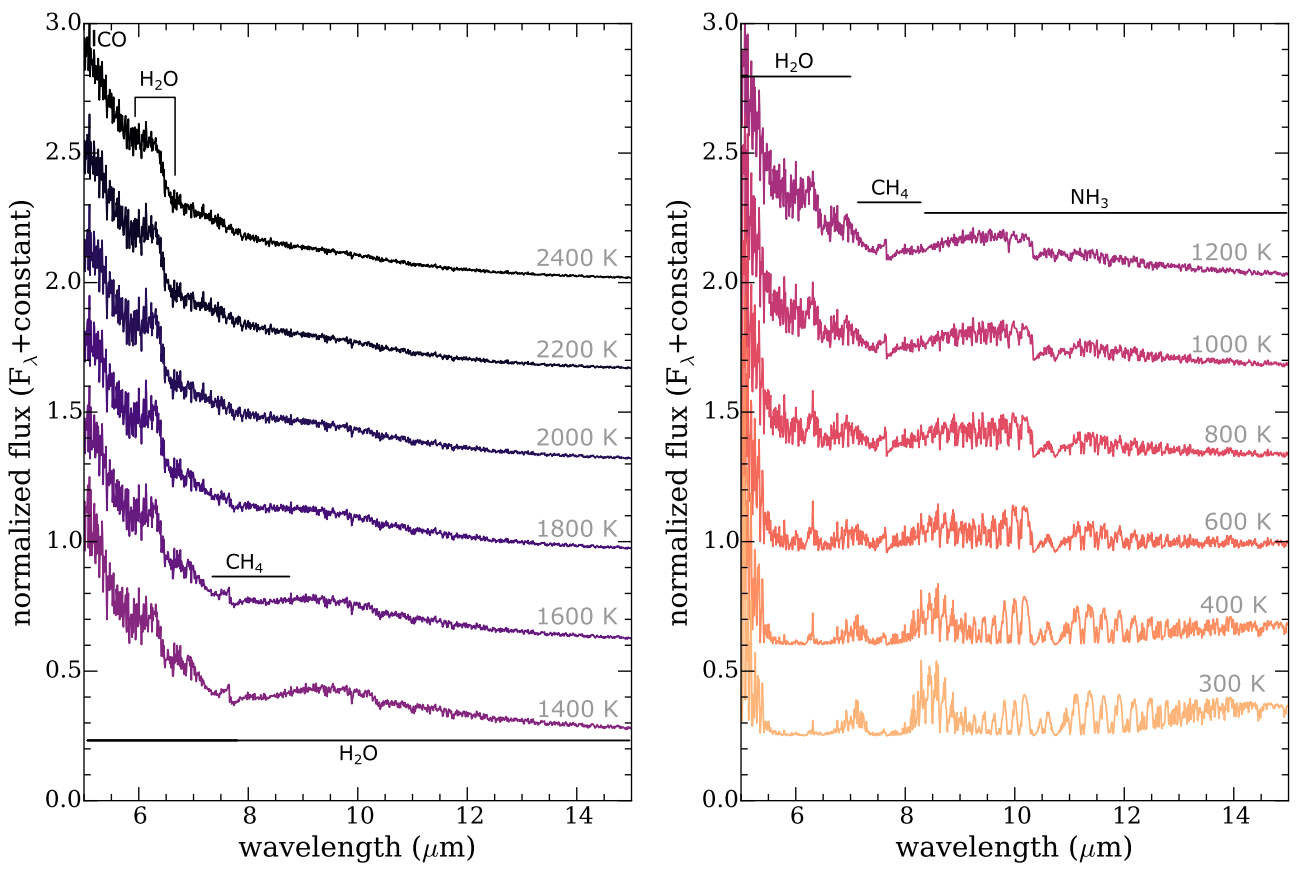


Figure 7. Same as Figure 3, but for the mid-IR spectral range with $R \sim 1000$. Note how the arrival of NH₃ dramatically transforms this region below about 1200 K in these equilibrium chemistry models.

molecular line lists generally are not similarly apparent at the illustrated spectral resolution $R \sim 1000$, but do appear at much higher spectral resolution R > 10,000.

3.3. Evolution

The newly computed evolution tracks are shown in Figures 10 and 11. The extension of the surface boundary condition to lower $T_{\rm eff}$ illuminates an interesting feature of Y-dwarf evolution. The SM08 models were based on atmospheres that extended only to 500 K and the corresponding boundary condition was extended to lower $T_{\rm eff}$ with a plausible, constrained extrapolation. That extrapolation was inaccurate because it did not account for the condensation of water, which the new low temperature atmosphere models include. As water is the dominant absorber in low $T_{\rm eff}$ Y dwarfs, its disappearance below $T_{\rm eff} < 400$ K results in more transparent atmospheres, which affects the evolution.

The impact of this accounting for water condensation can be seen in Figure 10 as a divergence in the respective cooling tracks of low-mass objects ($< 0.01\,M_\odot$) below $T_{\rm eff} \sim 400\,$ K. The new models have slightly higher gravity and luminosity (Figure 11). Qualitatively, this is similar to the hybrid model of SM08 for the L/T transition where the disappearance of cloud opacity causes a pileup of brown dwarfs at the transition (Kirkpatrick et al. 2021), although the effect appears to be weaker.

This result should not be taken at face value, however. The present cloudless model atmospheres include condensation of water but not the resulting cloud opacity. Unlike magnesium-silicate

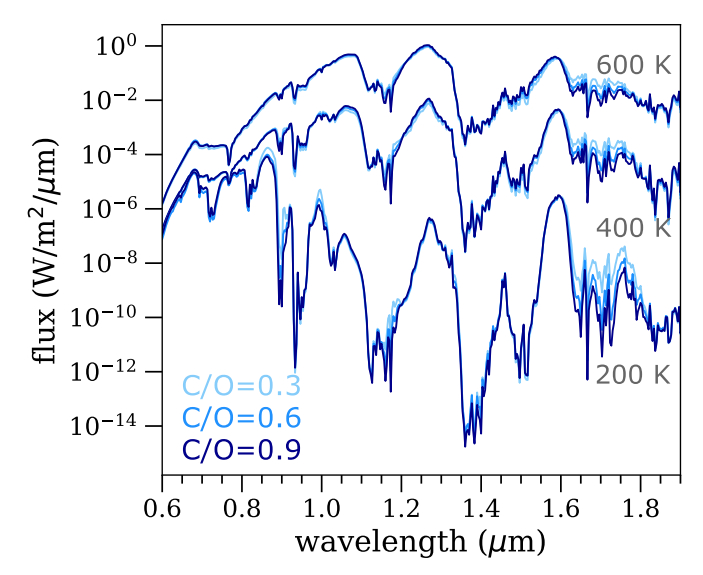


Figure 8. Comparison of model spectra ($R \sim 300$) for $\log g = 5$ at three $T_{\rm eff}$ and three C/O ratios as indicated. Note that the 400 and 200 K models have been scaled down by 10^2 and 10^4 , respectively, for clarity in plotting. Note that the indicated C/O ratios are for the bulk gas composition and not the gas composition in the photosphere probed here, as about 20% of the O atoms are lost to silicate-grain formation deeper in the atmosphere.

clouds, which have considerable opacity but whose gas phase precursors (e.g., MgH) have barely been detected in spectra (see, e.g., Kirkpatrick 2005) and thus have negligible opacity, water is the dominant gas-phase absorber throughout the L-T-Y sequence. Thus, water condensation transforms the opacity from

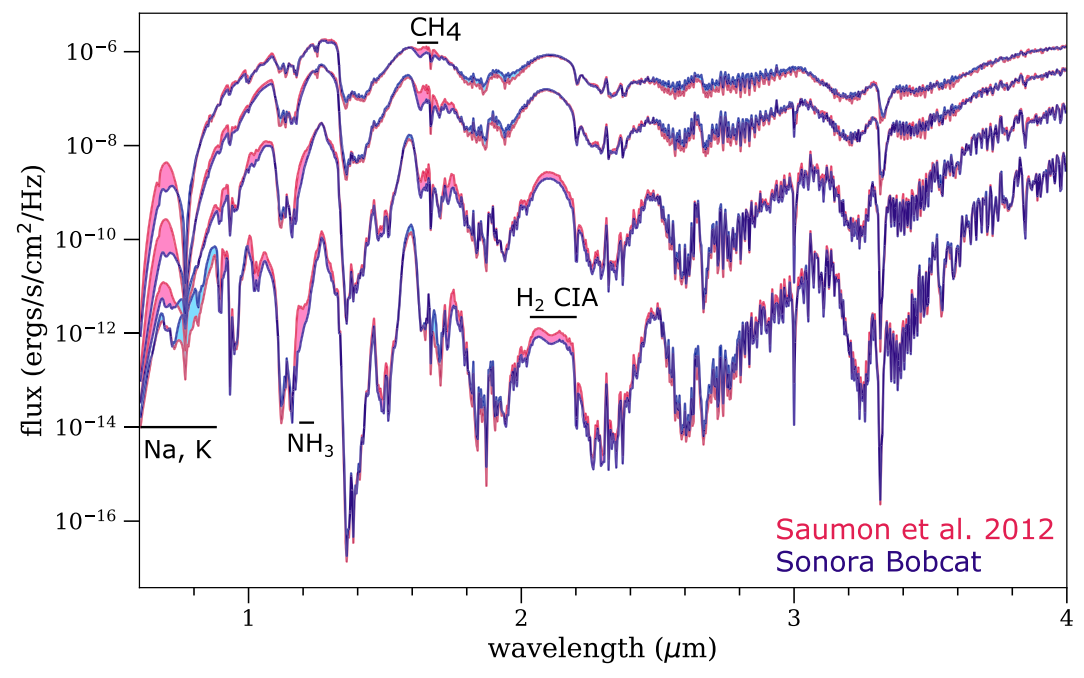


Figure 9. Comparison of the present Sonora Bobcat model spectra ($R \sim 1000$) with those of Saumon et al. (2012) at $T_{\rm eff} = 1300, 900, 500,$ and 300 K (top to bottom). Absorbers responsible for notable differences are labeled.

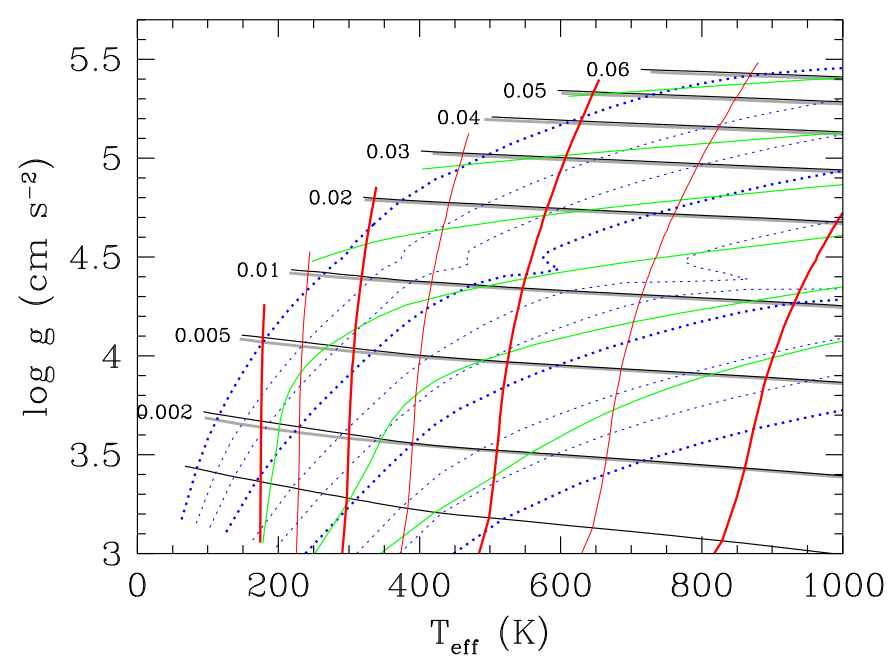


Figure 10. Low-temperature end of the cooling tracks of brown dwarfs in $T_{\rm eff}$ and gravity for the sequence based on cloudless atmospheres of solar metallicity. The evolution proceeds from right to left along the heavy black lines, which are labeled with the mass in M_{\odot} (the unlabeled track at the bottom has $M=0.001~M_{\odot}$). Light gray cooling tracks are from Saumon & Marley (2008). Isochrones are shown by the blue dotted lines: (from right to left) 0.01, 0.02, 0.04, 0.1, 0.2, 0.4, 1, 2, 4, and 10 Gyr. The nearly vertical red lines are curves of constant luminosity: (from left to right): $\log L/L_{\odot} = -8$, to -5 in steps of 0.5. Curves of constant radius are shown in green: (from top to bottom) 0.08 to 0.13 R_{\odot} in steps of 0.01. The phase of deuterium burning is revealed by the kink in the isochrones for objects with masses between 0.01 and 0.015 M_{\odot} .

a series of strong molecular bands throughout the near- and mid-IR to a continuum of condensate opacity. Until Y-dwarf models with a reliable description of water clouds are produced, the net effect of water condensation on very cool brown dwarf evolution will remain uncertain.

The effect of metallicity on the coolings tracks is shown in Figure 12 for the luminosity and Figure 13 for $T_{\rm eff}$. Generally, the higher-metallicity models are slightly more luminous at a

given age because the higher opacity of the atmosphere slows their cooling. All masses show the same trend with $\Delta \log L/\Delta [{\rm M/H}] \lesssim 0.15$. Deuterium burning causes the apparent anomalies in the 0.01 and $0.02\,M_\odot$ tracks. The $0.07\,M_\odot$ tracks are just below the hydrogen-burning minimum mass (HBMM). Since the HBMM decreases with increasing metallicity, the [M/H] = +0.5 model approaches a main-sequence equilibrium state while the others do not produce

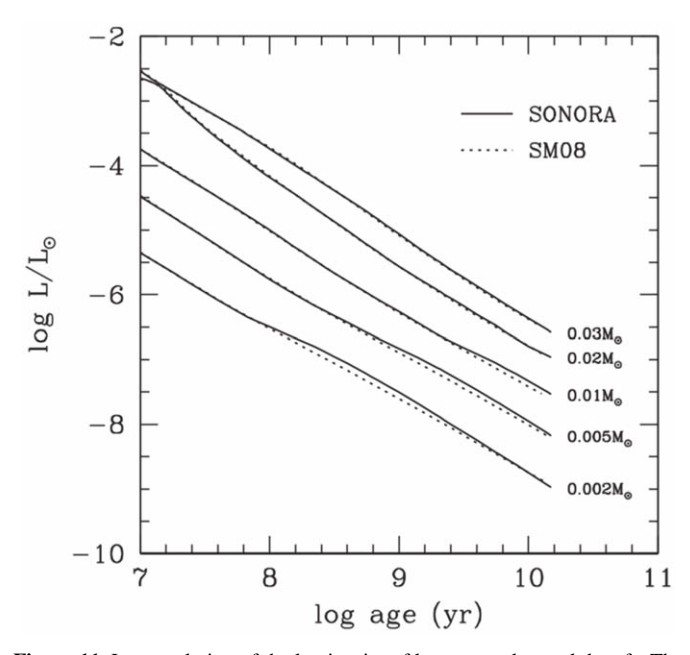


Figure 11. Late evolution of the luminosity of low-mass ultracool dwarfs. The present Sonora models (solid lines), include water condensation and remain more luminous (cool more slowly) below $T_{\rm eff} \sim 400~{\rm K}$ than the Saumon & Marley (2008) models (SM08, dotted lines). Each curve is labeled by the mass. The more massive dwarfs are not affected as they remain hotter than 400 K over the age of the Galaxy (see Figure 10).

enough nuclear energy to prevent further cooling. The evolution of $T_{\rm eff}$ is very similar to that of $L_{\rm bol}$.

Because of the systematic differences that persist between forward model spectra and data, determinations of $T_{\rm eff}$ and especially the gravity, by fitting observed spectra remain rather uncertain. Atmospheric parameters determined from models from different groups often disagree (e.g., Patience et al. 2012). However, the modeled bolometric luminosity, because it integrates over all wavelengths, is much less sensitive to such model errors and can also be determined fairly reliably from observations. Benchmark brown dwarfs, either bound in a binary system with a more easily characterized primary star or members of a moving group also have well determined metallicities and fairly well constrained ages. Equipped with $L_{\rm bol}$, [M/H] and the age, the mass (e.g. Figure 12), $T_{\rm eff}$, radius, and gravity follow from evolution sequences with a good degree of confidence.

The evolution sequences are available for all three metallicities. The tables provide mass, age, radius, luminosity, gravity, and $T_{\rm eff}$ along cooling tracks at constant mass and, for convenience, along isochrones, along constant luminosity curves, and for a given pair of $(T_{\rm eff}, \log g)$. The moment of inertia I is also provided for each mass as a function of time. For a spherically symmetric body of radius R,

$$I = \frac{8\pi}{3} \int_0^R \rho(r) r^4 dr$$

which is a useful quantity for studies of the angular momentum of brown dwarfs and their deformation under rotation (Barnes & Fortney 2003; Sengupta & Marley 2010; Jensen-Clem et al. 2020).

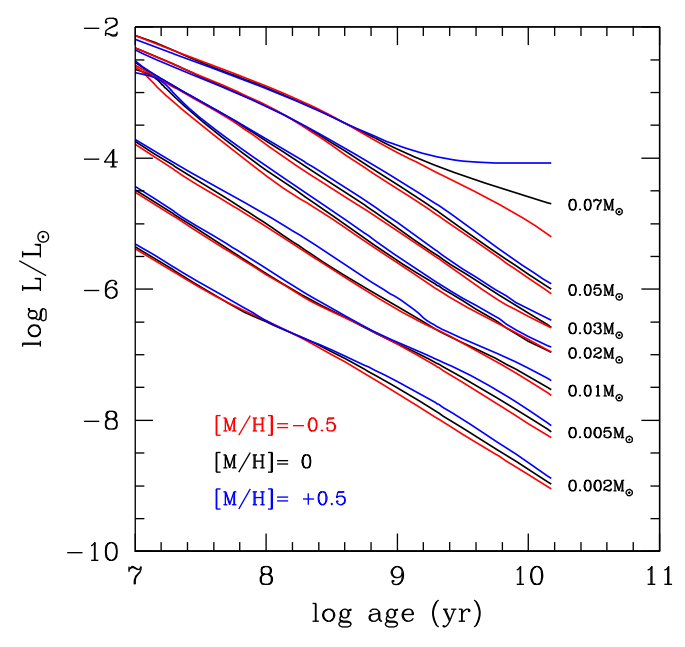


Figure 12. Comparison of brown dwarf luminosity cooling tracks for three different metallicities. Each triplet of tracks is labeled with the mass in solar masses. For a given mass and age, a higher metallicity results in a slightly higher luminosity. The $0.07\ M_{\odot}$ models are just below the hydrogen-burning minimum mass and their fates diverge after 2 Gyr, depending on the metallicity. The [M/H] = +0.5 track approaches a stable equilibrium on the main sequence while the lower metallicity tracks for that mass fail to do so.

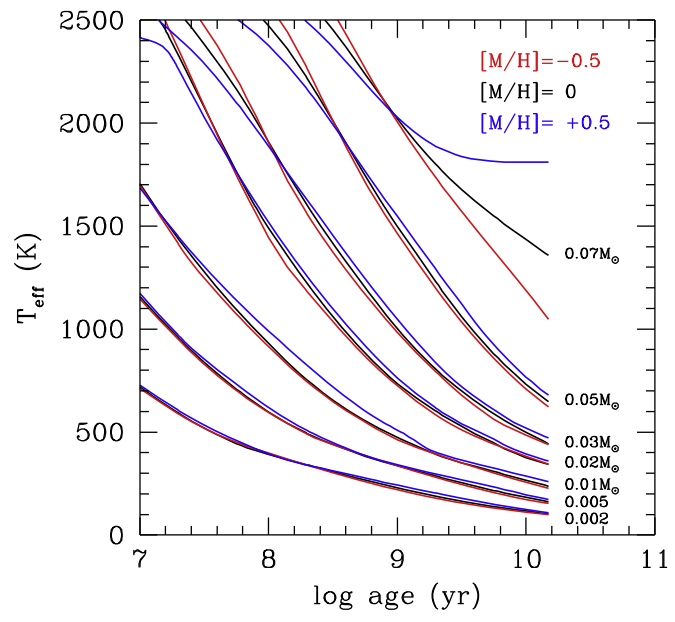


Figure 13. Same as Figure 12, but for the effective temperature.

4. Comparisons to Selected Data Sets

4.1. Spectra

Spectra from the Sonora Bobcat model set have already been used in a number of comparisons to various spectral data sets. The most systematic application has been in Zhang et al. (2021a) and Zhang et al. (2021b) who applied the Bayesian inference tool Starfish to near-infrared spectra ($R \sim 80$ –250) of 55 late-T dwarfs, including three benchmark (T7.5 and T8) objects. While good spectral fits could be found between model

¹⁷ https://doi.org/10.5281/zenodo.5063476

library and observed spectra, there were certain consistent discrepancies across most all objects. Most notably, the peak of the J-band in the best-fit spectra was too bright for most objects, while the peak of the H band was too dim. In both cases, the discrepancy increases with falling $T_{\rm eff}$ and later spectral types. Zhang et al. (2021b) attributed these discrepancies to deep clouds and disequilibrium chemistry, respectively, although further modeling is needed to understand this in detail.

Zhang et al. (2021b) also used this model set to quantify the well known degeneracy between metallicity and gravity by considering all of the model spectra. They found that the gravity-metallicity degeneracy can be described with $\Delta \log g \sim 3.42 \Delta [\text{M/H}]$. In other words, a change of +0.1 in [M/H] has nearly the same effect as a change in $\log g$ of about 0.34.

At higher spectral resolution, the models generally reproduce the finer spectral structure of cloudless objects fairly well. Comparing among three model sets, for example, Tannock et al. (2021) found Sonora-Bobcat models had the lowest χ^2 in J, H, and K bands when compared to $R \sim 6000$ spectra of a T7 dwarf; this is likely due to our choice of recent molecular opacity tables (Table 2) and illustrates the value of considerable effort that underlies the calculation of these tables.

4.2. Colors

The online tables contain model photometry in a selection of photometric passbands, including the MKO, WISE, SDSS, 2MASS, Spitzer/IRAC, and JWST systems. Model absolute magnitudes are computed using radii from the evolution model. Figure 14 shows our predicted Sonora Bobcat model photometry on the familiar ultracool dwarf J versus J-K colormagnitude diagram along with a sample of field dwarfs and subdwarfs selected from Best et al. (2020) for having well constrained photometry and distances. Model colors are shown for three gravities and three metallicities.

The models well reproduce the photometry of the latest M dwarfs and earliest L dwarfs, including the spread in J-K color. This is a substantial improvement over older evolution sets, which sometimes struggled over the same phase space, likely due to older H_2O opacities that lacked "hot" lines. By $J\sim 12$ the cloudless models turn to the blue instead of continuing to slide to the red as obseved in the field L-dwarf population, a consequence of the lack of dust opacity in these models. The [M/H] = +0.5 models are redder and make the turn about half a magnitude later. Conversely, the [M/H] = -0.5 are bluer in J-K from even brighter magnitudes, although the models of this metallicity are still not as blue as the majority of the M and L subdwarfs.

The best agreement with observed photometry is among the mid-T dwarfs, about T3 to T7, which are generally known to be well matched by cloudless model spectra (e.g., Marley et al. 1996). At still later spectral types the observed colors are again redder, likely a consequence of the formation of alkali clouds (Morley et al. 2012).

While there is a fair amount of structure in the individual tracks for each gravity and metallicity, generally speaking, lower metallicity models are always bluer than those with higher metallicity. This is a consequence of the J spectral bandpass being very sensitive to the total column gas opacity. At lower metallicities, flux from deep atmospheric layers emerges, keeping J magnitudes bright and J-K blue. As

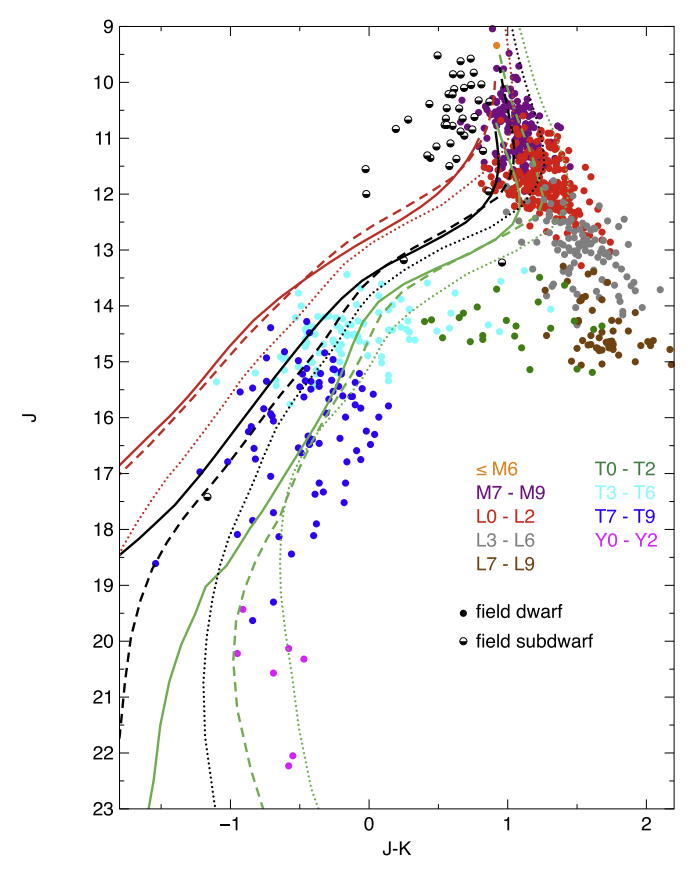


Figure 14. Sonora Bobcat cloudless colors for different constant values of gravity and metallicity as compared to Maunakea Observatory *J*- and *K*-band photometry of nearby M, L, T, and Y dwarfs from Best et al. (2020). The curves are coded by their line types (solid, dashed, dotted) for $\log g(\text{cm s}^{-2}) = 5$, 4, and 3, respectively, and line colors, from top to bottom groups [M/H] = -0.5, 0.0, and +0.5 for red, black, and green. The near-infrared spectral types are denoted by the color of the dot. Half-filled circles are subdwarfs.

metallicity increases, the J window closes as H_2O and other gas opacity squeeze in from the sides and the J-K contrast is reduced.

The dependence on gravity is generally more complex. Gravity affects the thermal profile, including the location and spacing of convection zones. The interaction of the changing thermal profile structure and the atmospheric opacity and chemistry alter the individual tracks for each gravity. Generally speaking, lower-gravity tracks are redder in J-K at all three metallicities.

Two additional color–magnitude diagrams in three JWST filters are shown in Figure 15. In this case, individual models are shown to better illustrate sensitivity to model parameters. F444W and F560W are commonly considered for substellar companion searches as they capture the 5 μ m excess flux seen in Figure 6. The color difference with F1000W shows a turn as the flux progressively moves redward with falling effective temperature. F444W – F1000W is reddest near 800 K while F560W – F1000W turns from red to blue at just a few hundred Kelvin.

4.3. Mass-radius Relationship

Intensive searches for transiting exoplanets over the past decade have uncovered many transiting brown dwarfs and giant planets, providing valuable determinations of the radius

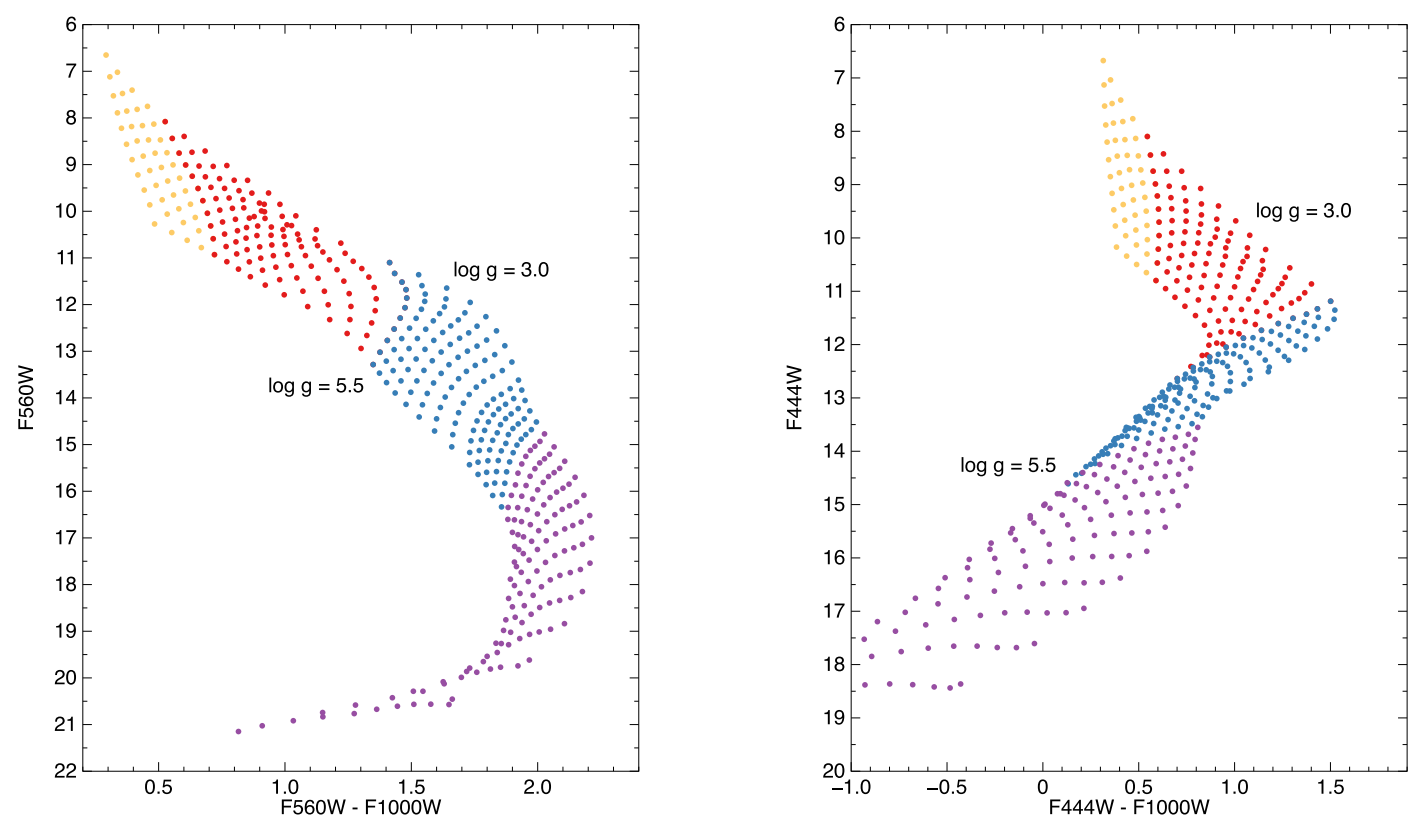


Figure 15. Color-magnitude diagrams in a selection of JWST mid-infrared filters, including two filters, F444W and F540W, commonly considered for searches for low-mass companions. Each individual point represents one solar metallicity model. Ranges of effective temperature are denoted by point color, from yellow (>2000 K) to red (2000 to 1000 K) to blue (1000 to 500 K) to purple (<500 K). Models are shown every 0.25 dex step in $\log g$ to illustrate sensitivity to parameters. Slight clumping among low-g models near 1700 K arises from numerical noise in those model temperature-pressure profiles.

of each object. In favorable cases, follow-up has led to the determination of the mass of the substellar companion. In addition, the characterization of the primary star of a system can constrain its age and its metallicity, giving a lower limit on the metal content of the companion. Combined with the orbital parameters, the degree of insolation in these relatively close binaries and any corresponding increases in radii can be estimated.

The mass-radius relation R(M) of very-low-mass stars, brown dwarfs, and giant planets has been extensively discussed and its main features were recognized early on (Burrows et al. 1989; Saumon et al. 1996). More recently, Stempels (2009) discussed the physics that drives its characteristic shape in detail and Burrows et al. (2011) explored the role of the helium abundance, metallicity, and clouds. Briefly, for ages greater than ~ 1 Gyr, the R(M) relation first rises in the Jupiter-mass range as the interior consists mostly of atomic/molecular fluid in the outer envelope and, deeper, a plasma where the electrons are moderately degenerate. Qualitatively, this corresponds to the regime of "normal matter" where the volume of an object increases with its mass. The radius peaks at $\sim 4 M_{\rm I}$ beyond which it declines steadily as most of the mass becomes a degenerate plasma and the R(M) relation behaves very much like that of white dwarfs (but with a hydrogen composition). When hydrogen fusion starts to contribute to the energy balance of the brown dwarfs, the star is partially supported by thermal pressure and the radius begins to rise again. For hydrogen-burning stars on the main sequence, the radius rises steadily with mass. Thus, the substellar R(M) relation of gaseous substellar objects has a local maximum around $4 M_{\rm J}$

and a minimum at 60–70 $M_{\rm J}$. It is remarkable that the radius of substellar objects remains within $\sim 15\%$ of $1\,R_{\rm J}$ for masses spanning two orders of magnitude (0.5–70 $M_{\rm J}$).

Figure 16 summarizes the mass-radius relation of our new models. Since brown dwarfs and exoplanets cool and contract with time, the R(M) relation is a function of time. The top panel of Figure 16 shows four isochrones of the R(M, t) relation for three different metallicities. While the older isochrones $(1-10 \,\mathrm{Gyr})$ display the behavior just discussed, the R(M)relation at 100 Myr is different. In particular, it does not show the inverse relation between radius and mass. The radius keeps rising with mass because the young, relatively hot objects are not supported by the pressure of degenerate electrons. There is also a prominent peak at $\sim 12 M_{\rm J}$ due to the short-lived phase of deuterium burning. This peak has almost vanished after 1 Gyr. The metallicity affects the radius in several ways. There are two dominant effects. A higher metallicity increases the opacity of the atmosphere and slows down the cooling and the contraction, so at a given M and age, the radius is larger. This matters primarily in the early evolution where the thermal content of the brown dwarf largely determines its radius. Another effect of the increased atmospheric opacity is that once nuclear fusion turns on, the flow of this additional energy to space is impeded, which is compensated for by a larger radius. This is significant for $M \gtrsim 0.06 \, M_{\odot}$ and ages of $\sim 1 \, \mathrm{Gyr}$ or more. Smaller effects include the change on the equation of state (see below) where increasing metallicity decreases the radius, primarily at late times of \sim 5 Gyr or more, and the effect of the condensation of water in the atmosphere decreases the

radius of these cloudless models (see Section 2.7), an effect that grows with the metallicity.

The middle panel of Figure 16 compares the present models with the cloudless, solar-metallicity models of SM08 for the same isochrones. The Sonora models are systematically smaller by \sim 1%–3%. This is due to the inclusion of metals in the equation of state (Equation (1)). The more massive objects shown eventually settle on the main sequence. The HBMM is indicated by the open circles for the 5 and 10 Gyr isochrones. Here, we define a main-sequence star as an object for which > 99.9% of the luminosity is provided by nuclear fusion. Lower-mass objects take a longer time to reach that limit if they are massive enough to reach it at all. Thus the HBMM decreases with time, as seen in the figure. Note that the HBMM is well above the location of the minimum radius of the isochrones. Objects that fall between the R(M, t) minimum and the HBMM are only partially supported by nuclear fusion $(L_{\text{nuclear}} < L_{\text{bol}}).$

The lower panel of Figure 16 compares the solar-metallicity Sonora models to data. The data points are colored according to the estimated age of each object and matched to the plotted isochrones (see caption for details). Although there are considerable uncertainties for several objects and the scatter is significant, the agreement is generally quite good. In most cases, outliers have larger radii than predicted by the models, which can be qualitatively explained by the role of stellar insolation as many of these objects are in very small orbits around their primary stars, with periods of just a few days. This radius increase can be compensated for by increasing the metallicity. A detailed comparison with the data, which would have to account for the metallicity and the effect of insolation of each object during its evolution, is beyond the scope of the present discussion. A few problematic objects remain that have radii smaller than predicted by the 10 Gyr isochrone. The most straightforward way to shrink an old brown dwarf or planet is to increase its metallicity, with the heavy elements dispersed throughout the body or concentrated in a core. Our models predict that a $0.05 M_{\odot}$ brown dwarf with 10 times the solar metallicity will see its radius decrease by $\sim 0.008\,$ R $_{\odot}$ at 5 and 10 Gyr, which is sufficient to reach even the smallest object shown in Figure 3. It is challenging to explain how such a massive object could acquire a metallicity that is well above that of its parent star.

The characteristics of the HBMM of the solar-metallicity Sonora models are nearly identical to those of the solarmetallicity cloudless SM08 models. For instance, the HBMM mass is $0.074 \, M_{\odot}$ (Sonora) compared to $0.075 \, M_{\odot}$ (SM08). As in SM08, we define the minimum mass for deuterium burning (DBMM) as the mass of an object that burns 90% of its initial deuterium content by the age of 10 Gyr. Again, we find a DBMM of 12.9 $M_{\rm J}$, which is nearly identical to the SM08 value of $13.1 M_{\rm J}$. At the DBMM, deuterium fusion can linger to $T_{\rm eff} \lesssim 800 \, {\rm K}$ but most of the deuterium is burned at higher temperatures ($T_{\rm eff} \gtrsim 1200~{\rm K}$) where clouds largely control the evolution. Deuterium fusion is likely to be affected by the process of cloud clearing at the L/T transition that occurs around 1200–1400 K (e.g., the hybrid model of SM08). The dependence on metallicity of the DBMM and HBMM of these cloudless models is of rather academic interests since it is well established that the HBMM occurs at $T_{\rm eff} \sim 1500 \, {\rm K}$ and that

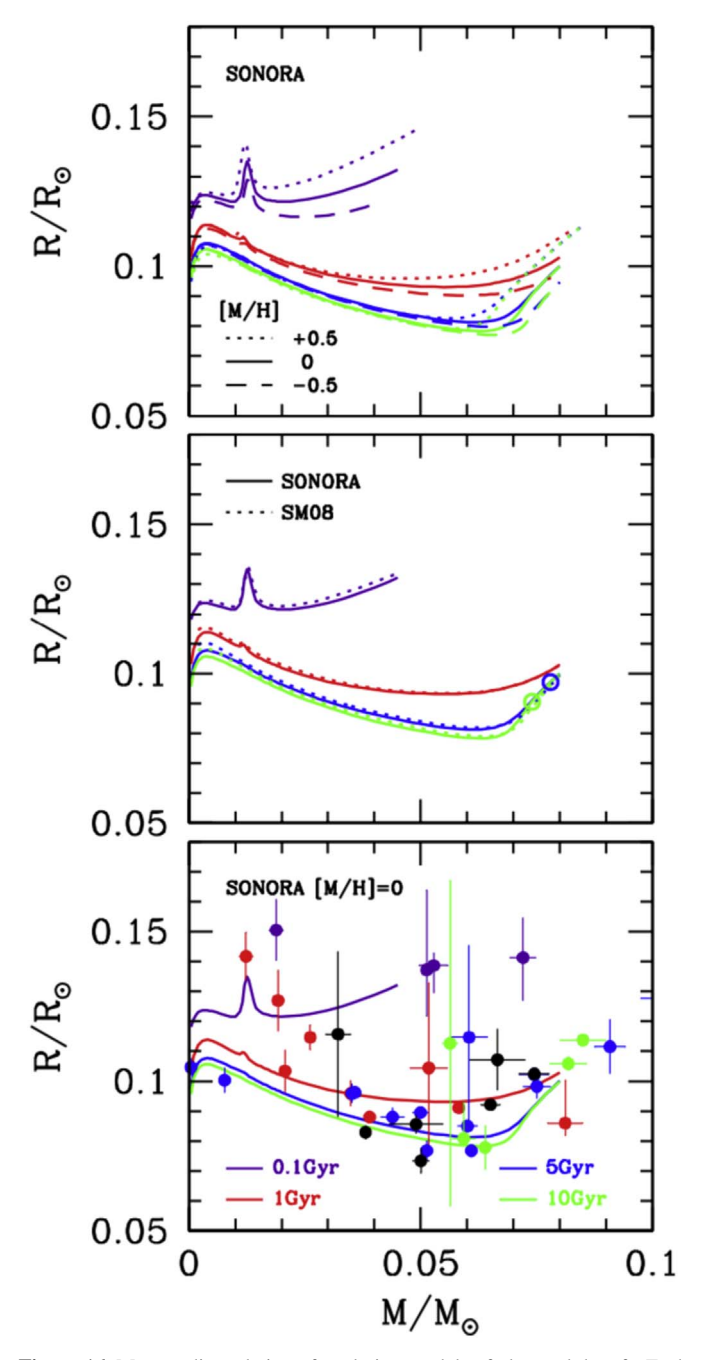


Figure 16. Mass-radius relation of evolution models of ultracool dwarfs. Each panel shows isochrones of the M-R relation: 0.1 Gyr (purple), 1 Gyr (red), 5 Gyr (blue), and 10 Gyr (green). Each isochrone is truncated at $T_{\rm eff} = 2400$ K, the limit of our atmosphere model grid. Top panel: dependence of the radius on the metallicity. Metal-rich objects have systematically larger radii because they cool more slowly. The sharp peak in the 100 Myr isochrone is caused by deuterium burning. Middle panel: comparison with the cloudless, solarmetallicity models of Saumon & Marley (2008; SM08). Large open circles indicate the location of the hydrogen-burning minimum mass for each isochrone. Bottom panel: comparison of solar-metallicity models with data. Data points are colored according to their age in bins corresponding to the model isochrones: 0.03–0.3 Gyr (purple), 0.3–2.2 Gyr (red), 2.2–7 Gyr (blue), >7 Gyr (green), unknown (black). Data from Winn et al. (2007), Littlefair et al. (2014), Gillen et al. (2017), Nowak et al. (2017), Parsons et al. (2017), von Boetticher et al. (2017), Cañas et al. (2018), Hodžić et al. (2018), Carmichael et al. (2019), David et al. (2019), Zhou et al. (2019), Acton et al. (2020), Benni et al. (2021), Carmichael et al. (2021), Casewell et al. (2020), Mireles et al. (2020), Šubjak et al. (2020), T.G. Beatty (2021, private communication), and S. L. Casewell (2021, private communication).

the bulk of deuterium is burned at $T_{\rm eff} \gtrsim 1200 \, \rm K$ with clouds playing an important role in both cases.

The characteristics of the models near the HBMM and DBMM are quite sensitive to the input physics of the models, mainly because of the extreme dependence of the nuclear fusion rates with temperature at these low temperatures where nuclear fusion reactions are marginal. This is illustrated by the evolution models of Fernandes et al. (2019) and Phillips et al. (2020) who make slightly different choices for the EOS. The former used EOS tables of carbon and oxygen as surrogates for all metals instead of an increased He mass fraction, and the latter used new EOS tables for H and He with an increased He mass fraction to represent the metals. In both studies, the models are very close to those of SM08, with small differences noticeable only near the HBMM and DBMM.

5. Conclusions

The forward modeling effort reported here represents another stepping stone in our efforts to understand the atmospheres and evolution of substellar objects. As molecular opacities have improved over the past decade, the limiting step in our understanding of their atmospheres now lies in atmospheric chemistry, mixing, and cloud processes. The models presented in this paper address the first of these. In upcoming papers, we will present new sets of models that explicitly explore disequilibrium chemistry and cloud processes.

The Sonora Bobcat models provide a comprehensive set of properties of cloudless models, including atmospheric (T, P)profiles, high-resolution spectra tailored to the capabilities of JWST, absolute magnitudes in all the bandpasses of key ground-based and space telescopes, and evolutionary tracks consistent with the model atmospheres. The models cover an expanded set of parameter space, most notably considering non-solar C/O and down to $T_{\rm eff} = 200$ K. The new models reach well into the $T_{\rm eff}$ range of spectral class Y and anticipates JWST discoveries of new objects nearly as cool as Jupiter.

The next set of models, by allowing for clouds in disequilibrium chemistry, will be better matched to the observed MLT sequence and will provide new insights into the L/T transition and L and T subdwarfs. A refined hybrid evolution model that accounts for the cloud clearing at the L/Ttransition will become possible. The number of well-characterized brown dwarfs is now large enough that comparisons with such a hybrid model will provide fresh insights into the L/T transition.

Further progress in the field will hinge on detailed, systematic comparisons of all available model sets to the wealth of observational data already available and soon to come from JWST. The combination of retrieval and forward model-fitting studies will illuminate where the atmosphere and evolution models excel and still fall short and provide essential clues as to the yet-to-be-discovered physics that are missing in forward models.

This work has made use of the VALD database, operated at Uppsala University, the Institute of Astronomy RAS in Moscow, and the University of Vienna. This work has benefited from The UltracoolSheet, maintained by Will Best, Trent Dupuy, Michael Liu, Rob Siverd, and Zhoujian Zhang, and developed from compilations by Dupuy & Liu (2012), Dupuy & Kraus (2013), Liu et al. (2016), Best et al. (2018), and Best et al. (2021). We thank Mike Liu for assistance with

preparing Figure 14 and general comments and Ivan Hubeny for helpful discussions on the various atmosphere modeling schools. Part of this work was performed under the auspices of the U.S. Department of Energy under Contract No. 89233218CNA000001.

ORCID iDs

Mark S. Marley https://orcid.org/0000-0002-5251-2943 Didier Saumon https://orcid.org/0000-0001-6800-3505 Roxana Lupu https://orcid.org/0000-0003-3444-5908 Richard Freedman https://orcid.org/0000-0001-9333-4306 Caroline Morley https://orcid.org/0000-0002-4404-0456 Jonathan J. Fortney https://orcid.org/0000-0002-9843-4354 Adam J. R. W. Smith https://orcid.org/0000-0002-9156-9651

D. J. Teal https://orcid.org/0000-0002-1912-3057 Ruoyan Wang https://orcid.org/0000-0002-4563-8919

```
References
Acton, J. S., Goad, M. R., Casewell, S. L., et al. 2020, MNRAS, 498, 3115
Allard, F., Allard, N. F., Homeier, D., et al. 2007a, A&A, 474, L21
Allard, F., Hauschildt, P. H., Alexander, D. R., Tamanai, A., & Schweitzer, A.
  2001, ApJ, 556, 357
Allard, F., Hauschildt, P. H., Baraffe, I., & Chabrier, G. 1996, ApJL, 465, L123
Allard, F., Hauschildt, P. H., & Schwenke, D. 2000, ApJ, 540, 1005
Allard, F., Homeier, D., & Freytag, B. 2014, in ASI Conf. Ser. 11, International
   Workshop on Stellar Spectral Libraries, ed. H. P. Singh, P. Prugniel, &
  I Vauglin (Pune, Maharashtra: ASI), 33
Allard, N. F., Kielkopf, J. F., & Allard, F. 2007b, EPJD, 44, 507
Allard, N. F., Spiegelman, F., & Kielkopf, J. F. 2016, A&A, 589, A21
Allard, N. F., Spiegelman, F., Leininger, T., & Molliere, P. 2019, A&A,
  628, A120
Amundsen, D. S., Tremblin, P., Manners, J., Baraffe, I., & Mayne, N. J. 2017,
   A&A, 598, A97
Arcangeli, J., Désert, J.-M., Line, M. R., et al. 2018, ApJL, 855, L30
Asplund, M., Amarsi, A. M., & Grevesse, N. 2021, A&A, 653, A141
Asplund, M., Grevesse, N., Sauval, A. J., & Scott, P. 2009, ARA&A, 47, 481
Azzam, A. A., Lodi, L., Yurchenko, S. N., & Tennyson, J. 2015, JQSRT,
Baraffe, I., Chabrier, G., Allard, F., & Hauschildt, P. H. 2002, A&A, 382, 563
Baraffe, I., Chabrier, G., Barman, T. S., Allard, F., & Hauschildt, P. H. 2003,
      A, 402, 701
Baraffe, I., Homeier, D., Allard, F., & Chabrier, G. 2015, A&A, 577, A42
Barber, R. J., Tennyson, J., Harris, G. J., & Tolchenov, R. N. 2006, MNRAS,
Barnes, J. W., & Fortney, J. J. 2003, ApJ, 588, 545
Barton, E. J., Yurchenko, S. N., & Tennyson, J. 2013, MNRAS, 434, 1469
Benni, P., Burdanov, A. Y., Krushinsky, V. V., et al. 2021, MNRAS,
Best, W. M. J., Liu, M. C., Magnier, E. A., & Dupuy, T. J. 2021, AJ, 161, 42
Best, W. M. J., Liu, M. C., Magnier, E. A., & Dupuy, T. J. 2020, AJ, 159, 257
Best, W. M. J., Magnier, E. A., Liu, M. C., et al. 2018, ApJS, 234, 1
Burcat, A., & Ruscic, B. 2005, Third millenium ideal gas and condensed
  phase thermochemical database for combustion (with update from
  active thermochemical tables) ANL-05/20, TAE 960, Argonne National
  Lab https://publications.anl.gov/anlpubs/2005/07/53802.pdf
Burningham, B., Marley, M. S., Line, M. R., et al. 2017, MNRAS, 470, 1177
Burningham, B., Faherty, J. K., Gonzales, E. C., et al. 2021, MNRAS,
   506, 1944
Burrows, A., Burgasser, A. J., Kirkpatrick, J. D., et al. 2002, ApJ, 573, 394
Burrows, A., Heng, K., & Nampaisarn, T. 2011, ApJ, 736, 47
Burrows, A., Hubbard, W. B., & Lunine, J. I. 1989, ApJ, 345, 939
Burrows, A., Hubbard, W. B., Lunine, J. I., & Liebert, J. 2001, RvMP, 73, 719
Burrows, A., Hubeny, I., Hubbard, W. B., Sudarsky, D., & Fortney, J. J. 2004,
   ApJL, 610, L53
Burrows, A., Marley, M. S., & Sharp, C. M. 2000a, ApJ, 531, 438
Burrows, A., Marley, M. S., & Sharp, C. M. 2000b, ApJ, 531, 438
Burrows, A., Sudarsky, D., & Hubeny, I. 2006, ApJ, 650, 1140
Burrows, A., Marley, M., Hubbard, W. B., et al. 1997, ApJ, 491, 856
```

Cañas, C. I., Bender, C. F., Mahadevan, S., et al. 2018, ApJL, 861, L4

```
Caffau, E., Ludwig, H.-G., Steffen, M., Freytag, B., & Bonifacio, P. 2011,
   SoPh, 268, 255
Carmichael, T. W., Latham, D. W., & Vanderburg, A. M. 2019, AJ, 158, 38
Carmichael, T. W., Quinn, S. N., Zhou, G., et al. 2021, AJ, 161, 97
Casewell, S. L., Belardi, C., Parsons, S. G., et al. 2020, MNRAS, 497, 3571
Chabrier, G., & Baraffe, I. 1997, A&A, 327, 1039
Chandrasekhar, S., & Münch, G. 1946, ApJ, 104, 446
Chase, M. W. 1998, Journal of Physical and Chemical Reference Data, 28,
   Monograph No. 9 (Woodbury, NY: AIP)
Cushing, M. C., Marley, M. S., Saumon, D., et al. 2008, ApJ, 678, 1372
David, T. J., Hillenbrand, L. A., Gillen, E., et al. 2019, ApJ, 872, 161
Dulick, M. C. W., Bauschlicher, J., Burrows, A., et al. 2003, ApJ, 594, 651
Dupuy, T. J., & Kraus, A. L. 2013, Sci, 341, 1492
Dupuy, T. J., & Liu, M. C. 2012, ApJS, 201, 19
Dupuy, T. J., & Liu, M. C. 2017, ApJS, 231, 15
Fegley, B. J., & Lodders, K. 1994, Icar, 110, 117
Fegley, B. J., & Lodders, K. 1996, ApJL, 472, L37
Fernandes, C. S., Van Grootel, V., Salmon, S. J. A. J., et al. 2019, ApJ, 879, 94
Fortney, J. J., Ikoma, M., Nettelmann, N., Guillot, T., & Marley, M. S. 2011,
    ApJ, 729, 32
Fortney, J. J., Marley, M. S., Lodders, K., Saumon, D., & Freedman, R. 2005,
   ApJL, 627, L69
Fortney, J. J., Marley, M. S., Saumon, D., & Lodders, K. 2008, ApJ, 683, 1104
Fortney, J. J., Mordasini, C., Nettelmann, N., et al. 2013, ApJ, 775, 80
Freedman, R. S., Lustig-Yaeger, J., Fortney, J. J., et al. 2014, ApJS, 214, 25
Freedman, R. S., Marley, M. S., & Lodders, K. 2008, ApJS, 174, 504
Garland, R., & Irwin, P. G. J. 2019, arXiv:1903.03997
Gharib-Nezhad, E., Marley, M. S., Batalha, N. E., et al. 2021, ApJ, 919, 21
Gillen, E., Hillenbrand, L. A., David, T. J., et al. 2017, ApJ, 849, 11
Gordon, S., & McBride, B. J. 1994, Computer Program for Calculation of
   Complex Chemical Equilibrium Compositions and Applications, NASA
   Reference Publication 1311, https://ntrs.nasa.gov/api/citations/
   19950013764/downloads/19950013764.pdf
Gurvich, L. V., Veyts, I. V., & Alcock, C. B. 1989, Thermodynamic Properties
   of Individual Substances (4th ed.; New York: Hemisphere Publishing)
Gurvich, L. V., Veyts, I. V., & Alcock, C. B. 1991, Thermodynamic Properties
   of Individual Substances, Vol. 2 (4th ed.; New York: Hemisphere
   Publishing)
Gurvich, L. V., Veyts, I. V., & Alcock, C. B. 1994, Thermodynamic Properties
   of Individual Substances, Vol. 3 (4th ed.; Boca Raton, FL: CRC Press)
Hargreaves, R. J., Hinkle, K. H., Bauschlicher, C. W., et al. 2010, AJ, 140, 919
Harris, G. J., Larner, F. C., Tennyson, J., et al. 2008, MNRAS, 390, 143
Harris, G. J., Tennyson, J., Kaminsky, B. M., Pavlenko, Y. V., &
  Jones, H. R. A. 2006, MNRAS, 367, 400
Heng, K., & Kitzmann, D. 2017, ApJS, 232, 20
Heng, K., Lyons, J. R., & Tsai, S.-M. 2016, ApJ, 816, 96
Hodžić, V., Triaud, A. H. M. J., Anderson, D. R., et al. 2018, MNRAS,
   481, 5091
Huang, X., Gamache, R. R., Freedman, R. S., Schwenke, D. W., & Lee, T. J.
  2014, JOSRT, 147, 134
Hubeny, I. 1988, CoPhC, 52, 103
Hubeny, I. 2017, MNRAS, 469, 841
Hubeny, I., & Burrows, A. 2007, ApJ, 669, 1248
Hubeny, I., & Lanz, T. 1995, ApJ, 439, 875
Hubeny, I., & Mihalas, D. 2014, Theory of Stellar Atmospheres (Princeton, NJ:
   Princeton Univ. Press)
Jensen-Clem, R., Millar-Blanchaer, M. A., van Holstein, R. G., et al. 2020, AJ,
   160, 286
Joergens, V. 2014, 50 Years of Brown Dwarfs: From Prediction to Discovery
   to Forefront of Research, Vol. 401 (Cham: Springer)
Kataria, T., Sing, D. K., Lewis, N. K., et al. 2016, ApJ, 821, 9
Kirkpatrick, J. D. 2005, ARA&A, 43, 195
Kirkpatrick, J. D., Gelino, C. R., Faherty, J. K., et al. 2021, ApJS, 253, 7
Kissel, A., Sumpf, B., Kronfeldt, H.-D., Tikhomirov, B., & Ponomarev, Y.
  2002, JMoSp, 216, 345
Kitzmann, D., Heng, K., Oreshenko, M., et al. 2020, ApJ, 890, 174
Kurucz, R. L. 2011, CaJPh, 89, 417
Kurucz, R. L., & Avrett, E. H. 1981, SAOSR, 391
Lacis, A. A., & Oinas, V. 1991, JGR, 96, 9027
Li, G., Gordon, I. E., Rothman, L. S., et al. 2015, ApJS, 216, 15
Liebert, J., Reid, I. N., Burrows, A., et al. 2000, ApJL, 533, L155
Line, M. R., Teske, J., Burningham, B., Fortney, J. J., & Marley, M. S. 2015,
    pJ, 807, 183
Line, M. R., Marley, M. S., Liu, M. C., et al. 2017, ApJ, 848, 83
Littlefair, S. P., Casewell, S. L., Parsons, S. G., et al. 2014, MNRAS, 445, 2106
Liu, M. C., Dupuy, T. J., & Allers, K. N. 2016, ApJ, 833, 96
```

```
Lodders, K. 1999, ApJ, 519, 793
Lodders, K. 2002, ApJ, 577, 974
Lodders, K. 2010, in Formation and Evolution of Exoplanets, ed. R. Barnes
   (New York: Wiley), 157
Lodders, K. 2020, Oxford Research Encyclopedia of Planetary Science
   (Oxford: Oxford Univ. Press)
Lodders, K., & Fegley, B. 2002, Icar, 155, 393
Lodders, K., & Fegley, B. 2006, Astrophysics Update 2, Springer Praxis Books
   (Berlin: Springer)
Lupu, R. E., Zahnle, K., Marley, M. S., et al. 2014, ApJ, 784, 27
Malik, M., Grosheintz, L., Mendonça, J. M., et al. 2017, AJ, 153, 56
Marley, M. S., Fortney, J. J., Hubickyj, O., Bodenheimer, P., & Lissauer, J. J.
   2007, ApJ, 655, 541
Marley, M. S., Gelino, C., Stephens, D., Lunine, J. I., & Freedman, R. 1999,
   ApJ, 513, 879
Marley, M. S., & Robinson, T. D. 2015, ARA&A, 53, 279
Marley, M. S., Saumon, D., Cushing, M., et al. 2012, ApJ, 754, 135
Marley, M. S., Saumon, D., Guillot, T., et al. 1996, Sci, 272, 1919
Marley, M. S., Seager, S., Saumon, D., et al. 2002, ApJ, 568, 335
Marois, C., Macintosh, B., Barman, T., et al. 2008, Sci, 322, 1348
McKay, C. P., Pollack, J. B., & Courtin, R. 1989, Icar, 80, 23
McKemmish, L. K., Yurchenko, S. N., & Tennyson, J. 2016, MNRAS,
  463, 771
Miles, B. E., Skemer, A. J. I., Morley, C. V., et al. 2020, AJ, 160, 63
Mireles, I., Shporer, A., Grieves, N., et al. 2020, AJ, 160, 133
Morley, C. V., Fortney, J. J., Kempton, E. M.-R., et al. 2013, ApJ, 775, 33
Morley, C. V., Fortney, J. J., Marley, M. S., et al. 2012, ApJ, 756, 172
Morley, C. V., Marley, M. S., Fortney, J. J., & Lupu, R. 2014a, ApJL, 789, L14
Morley, C. V., Marley, M. S., Fortney, J. J., et al. 2014b, ApJ, 787, 78
Morley, C. V., Skemer, A. J., Miles, B. E., et al. 2019, ApJL, 882, L29
Moses, J. I., Line, M. R., Visscher, C., et al. 2013, ApJ, 777, 34
Nowak, G., Palle, E., Gandolfi, D., et al. 2017, AJ, 153, 131
Oppenheimer, B. R., Kulkarni, S. R., Matthews, K., & Nakajima, T. 1995, Sci,
Orton, G., Ortiz, J. L., Baines, K., et al. 1996, Sci, 272, 839
Parsons, S. G., Hermes, J. J., Marsh, T. R., et al. 2017, MNRAS, 471, 976
Patience, J., King, R. R., De Rosa, R. J., et al. 2012, A&A, 540, A85
Phillips, M. W., Tremblin, P., Baraffe, I., et al. 2020, A&A, 637, A38
Piette, A. A. A., & Madhusudhan, N. 2020, MNRAS, 497, 5136
Pine, A. S. 1992, JChPh, 97, 773
Potekhin, A. Y., & Chabrier, G. 2012, A&A, 538, A115
Robie, R. A., & Hemingway, B. S. 1995, Thermodynamic Properties of
   Minerals and Related Substances at 298.15 K and 1 Bar (10<sup>5</sup> Pascals)
   Pressure and at Higher Temperatures (USGS Bulletin 2131) (Reston, VA:
   U.S. Geological Survey), https://pubs.usgs.gov/bul/2131/report.pdf
Robinson, T. D., & Catling, D. C. 2014, NatGe, 7, 12
Rossi, F., & Pascale, J. 1985, PhRvA, 32, 2657
Rothman, L., Gordon, I., Barber, R., et al. 2010, JQSRT, 111, 2139
Rothman, L. S., Gordon, I. E., Babikov, Y., et al. 2013, QSRT, 130, 4
Ryabchikova, T., Piskunov, N., Kurucz, R., et al. 2015, PhyS, 90, 054005
Salem, J., Bouanich, J.-P., Walrand, J., Aroui, H., & Blanquet, G. 2004,
  JMoSp, 228, 23
Saumon, D., Chabrier, G., & van Horn, H. M. 1995, ApJS, 99, 713
Saumon, D., Hubbard, W. B., Burrows, A., et al. 1996, ApJ, 460, 993
Saumon, D., & Marley, M. S. 2008, ApJ, 689, 1327
Saumon, D., Marley, M. S., Abel, M., Frommhold, L., & Freedman, R. S.
   2012, ApJ, 750, 74
Schwenke, D. W. 1998, FaDi, 109, 321
Sengupta, S., & Marley, M. S. 2010, ApJL, 722, L142
Skemer, A. J., Morley, C. V., Allers, K. N., et al. 2016, ApJL, 826, L17
Sousa-Silva, C., Al-Refaie, A. F., Tennyson, J., & Yurchenko, S. N. 2015,
   MNRAS, 446, 2337
Stempels, E. 2009, in AIP Conf. Ser. 1094, Proc. of the 15th Cambridge
   Workshop on Cool Stars, Stellar Systems and the Sun, ed. E. Stempels
   (Melville, NY: AIP), 102
Stephens, D. C., Leggett, S. K., Cushing, M. C., et al. 2009, ApJ, 702, 154
Tannock, M. E., Metchev, S., Heinze, A., et al. 2021, AJ, 161, 224
Tennyson, J., & Yurchenko, S. 2018, Atoms, 6, 26
Tennyson, J., & Yurchenko, S. N. 2012, MNRAS, 425, 21
Toon, O. B., McKay, C. P., Ackerman, T. P., & Santhanam, K. 1989, JGR, 94,
   16287
Visscher, C. 2012, ApJ, 757, 5
Visscher, C., Lodders, K., & Fegley, B., Jr. 2010, ApJ, 716, 1060
Visscher, C., Lodders, K., & Fegley, B. J. 2006, ApJ, 648, 1181
von Boetticher, A., Triaud, A. H. M. J., Queloz, D., et al. 2017, A&A, 604, L6
Šubjak, J., Sharma, R., Carmichael, T. W., et al. 2020, AJ, 159, 151
```

- Wakeford, H. R., Visscher, C., Lewis, N. K., et al. 2017, MNRAS, 464, 4247
 Weck, P. F., Schweitzer, A., Kirby, K., Hauschildt, P. H., & Stancil, P. C. 2004, ApJ, 613, 567
- Weck, P. F., Schweitzer, A., Stancil, P. C., Hauschildt, P. H., & Kirby, K. 2003, ApJ, 582, 1059
- Wilzewski, J., Gordon, I., Kochanov, R., Hill, C., & Rothman, L. 2016, JQSRT, 168, 193
- Winn, J. N., Holman, M. J., Henry, G. W., et al. 2007, AJ, 133, 1828 Yurchenko, S. N., Barber, R. J., & Tennyson, J. 2011, MNRAS, 413, 1828
- Yurchenko, S. N., & Tennyson, J. 2014, MNRAS, 440, 1649
- Yurchenko, S. N., Tennyson, J., Barber, R. J., & Thiel, W. 2013, JMoSp, 291, 69
- Zalesky, J. A., Line, M. R., Schneider, A. C., & Patience, J. 2019, ApJ, 877, 24
 Zhang, Z., Liu, M. C., Marley, M. S., Line, M. R., & Best, W. M. J. 2021a, ApJ, 916, 53
- Zhang, Z., Liu, M. C., Marley, M. S., Line, M. R., & Best, W. M. J. 2021b, ApJ, in press, arXiy:2105.05256
- Zhou, G., Bakos, G. Á., Bayliss, D., et al. 2019, AJ, 157, 31